



**HAL**  
open science

# Reconstructing matter profiles of spherically compensated cosmic regions in $\Lambda$ CDM cosmology

Paul de Fromont, Jean-Michel Alimi

► **To cite this version:**

Paul de Fromont, Jean-Michel Alimi. Reconstructing matter profiles of spherically compensated cosmic regions in  $\Lambda$ CDM cosmology. Monthly Notices of the Royal Astronomical Society, 2018, 473 (4), pp.5177-5194. 10.1093/mnras/stx2677 . hal-01758670

**HAL Id: hal-01758670**

**<https://hal.science/hal-01758670v1>**

Submitted on 3 May 2023

**HAL** is a multi-disciplinary open access archive for the deposit and dissemination of scientific research documents, whether they are published or not. The documents may come from teaching and research institutions in France or abroad, or from public or private research centers.

L'archive ouverte pluridisciplinaire **HAL**, est destinée au dépôt et à la diffusion de documents scientifiques de niveau recherche, publiés ou non, émanant des établissements d'enseignement et de recherche français ou étrangers, des laboratoires publics ou privés.

# Reconstructing matter profiles of spherically compensated cosmic regions in $\Lambda$ CDM cosmology

Paul de Fromont<sup>★</sup> and Jean-Michel Alimi

*LUTH, Observatoire de Paris, PSL Research University, CNRS, Université Paris Diderot, Sorbonne Paris Cité, 5 place Jules Janssen, F-92195 Meudon, France*

Accepted 2017 October 10. Received 2017 October 10; in original form 2017 July 17

## ABSTRACT

The absence of a physically motivated model for large-scale profiles of cosmic voids limits our ability to extract valuable cosmological information from their study. In this paper, we address this problem by introducing the spherically compensated cosmic regions, named CoSpheres. Such cosmic regions are identified around local extrema in the density field and admit a unique compensation radius  $R_1$  where the internal spherical mass is exactly compensated. Their origin is studied by extending the standard peak model and implementing the compensation condition. Since the compensation radius evolves as the Universe itself,  $R_1(t) \propto a(t)$ , CoSpheres behave as bubble Universes with fixed comoving volume. Using the spherical collapse model, we reconstruct their profiles with a very high accuracy until  $z = 0$  in  $N$ -body simulations. CoSpheres are symmetrically defined and reconstructed for both central maximum (seeding haloes and galaxies) and minimum (identified with cosmic voids). We show that the full non-linear dynamics can be solved analytically around this particular compensation radius, providing useful predictions for cosmology. This formalism highlights original correlations between local extremum and their large-scale cosmic environment. The statistical properties of these spherically compensated cosmic regions and the possibilities to constrain efficiently both cosmology and gravity will be investigated in companion papers.

**Key words:** dark energy – large-scale structure of Universe – cosmology: theory.

## 1 INTRODUCTION

One of the main purpose of modern cosmology is to understand the nature of Dark Energy (DE), driving the cosmic acceleration (Riess et al. 1998; Perlmutter et al. 1999; Caldwell & Kamionkowski 2009; Silvestri & Trodden 2009). It is not only difficult to build consistent models to understand this acceleration but rather to find binding limits to discriminates between them.

Large-scale structures (LSS) offer a large panel of probes for cosmology and the nature of gravity itself. They carry informations on both primordial Universe and gravity through the cosmological evolution. These last years, cosmic structure formation have been specially studied in the frame of cosmic voids formation and statistics (Park & Lee 2007; Lavaux & Wandelt 2012; Pan et al. 2012; Cai, Padilla & Li 2015; Hamaus et al. 2015, 2016; Achitouv 2017; Achitouv et al. 2017). Although cosmic void dynamics is far from being linear, these regions are safe from the highly non-linear physics occurring during haloes or galaxy formation. Moreover, cosmic voids are expected to be more sensitive to the nature of DE since their local  $\Omega_{\text{DE}}$  is higher than in the average Universe (Sheth & van de Weygaert 2004; Colberg et al. 2005; van

de Weygaert & Platen 2011). Voids have been studied through the Alcock–Paczynski test (Sutter et al. 2014; Mao et al. 2017), their ellipticity (Park & Lee 2007; Lavaux & Wandelt 2010) and their abundance or shape (Cai et al. 2015; Achitouv et al. 2016). However, all these studies suffer from the lack of a fully consistent – and physically motivated – model describing both the origin and the dynamical generation of such cosmic regions. Hamaus, Sutter & Wandelt (2014b) introduced an effective parametrization of density profiles using numerical simulation. Despite not being deduced from first principles, it can provide physical insights. For example, Hamaus et al. (2016) used it to model the isotropic shape of the void-density profile and have been able to isolate the sensibility to cosmological parameters through anisotropic redshift-space and Alcock–Paczynski distortions.

In this paper and through the following ones (Alimi & de Fromont 2017a,b; de Fromont & Alimi 2017), we present a physically motivated model studying both the primordial origin and the dynamical evolution of such cosmic regions. More precisely, we generalize cosmic void study by introducing the spherically compensated cosmic regions, named thereafter CoSpheres.<sup>1</sup> These structures are defined as the large-scale cosmic environment

<sup>★</sup> E-mail: paul.de-fromont@obspm.fr

<sup>1</sup> For Compensated Spherical regions.

surrounding local extrema of the density field. When defined around central under-densities (local minimum), these regions can be identified to cosmic voids. Interestingly, these regions can also be defined around central overdense maxima, defining the symmetric of standard voids.

In average,<sup>2</sup> the large-scale environment around maxima (respectively minima) in the density field can be separated in two distinct domains: an internal over (respectively under) dense core surrounded by a large under (respectively over) dense compensation belt. Note that even if the density field around local extrema is far from being spherical, one can always define a spherical profile by averaging over angles. However, despite being intuitive, the density contrast  $\delta(\mathbf{x}) = \rho(\mathbf{x})/\bar{\rho}_m - 1$  has no dynamical interpretation. Indeed, in the spherical frame, the local gravitational dynamics is driven by the integrated density contrast, or equivalently the mass contrast

$$\Delta(r) = \frac{3}{r^3} \int_0^r u^2 \delta(u) du = \frac{m(r)}{4\pi/3 \bar{\rho}_m r^3} - 1. \quad (1)$$

Like for density, the large-scale environment of local extrema can be splitted in an overmassive (respectively undermassive for central minima) core surrounded by an undermassive (respectively overmassive) area. The transition radius between these under-/overmassive regions defines the compensation radius, noted  $R_1$ . This radius can be uniquely define for each central extrema.<sup>3</sup> In a naive spherical description, this radius separates the collapsing over-massive region from the expanding undermassive one. The existence of such scale is fundamentally ensured by the Bianchi identities (Hehl & Mccrea 1986) which impose the mass conservation. Moreover, the compensation radius  $R_1$  follows a remarkable evolution. Indeed, since  $R_1$  encloses a sphere whose averaged density equals the background density, it evolves as the scale factor itself, i.e.  $R_1(t) \propto a(t)$ . CoSpheres thus behave as bubble universes with a fixed comoving size. Hamaus et al. (2014a) introduced a similar concept of a compensation radius for voids and its use as a static cosmological ruler that follows the background expansion. However, our definition of the compensation radius differs since it is defined uniquely for each maximum (see equation 5). We also stress that, on the Hubble size, there should not ‘overcompensated’ or ‘undercompensated’ voids as a consequence of the mass conservation.

The LSS are originally generated by the stochastic fluctuations of the density field in the primordial Universe. Their statistical properties, including average shape and probability distribution can be computed within the Gaussian random field (GRF) formalism. However, it is necessary to implement the compensation constraint (the existence of a finite compensation radius  $R_1$ ) and thus to extend the results of Bardeen et al. (1986). As we show in this paper, the non-linear evolution of such regions is very well described by using the spherical collapse (SC) model while neither Zel’dovich nor Eulerian linear dynamics is accurate enough.

We discuss the linear scaling of the density profiles of such regions in both primordial and evolved Universe. It turns out that these large-scale profiles do not scale linearly on  $R_1$ , neither on shape nor amplitude. This property emerges from the fact that on scales considered here (from  $r \sim 5$  to  $r \geq 100 h^{-1}$  Mpc), the linear matter power spectrum is far from being scale invariant. Moreover,

the non-linear gravitational evolution of these profiles would have broken any primordial linear scaling.

The paper is organized as follow. In Section 2, we introduce the  $N$ -body simulations on which is based our study; the ‘Dark Energy Universe Simulations (DEUS) (see Section 2.1). After defining precisely CoSpheres, we study these regions in the numerical simulations for various redshift and sizes and for both central over- and underdensities. This leads us to discuss the stacking method used to reconstruct the corresponding average profiles.

In Section 3, we study the shape of these regions in a Gaussian primordial field. We present an extension of the usual peak formalism of BBKS (Bardeen et al. 1986). While BBKS formalism focuses on the local properties of the field around the peak (note that for us, a peak is an extremum and can be a minimum or a maximum), we extend this model to take into account its cosmic environment on large scale. We show that this environment can be fully qualified by the compensation scale  $R_1$  and the compensation density  $\delta_1 = \delta(R_1)$ .

In Section 4, we study the dynamical evolution of CoSpheres. We show that the Lagrangian SC model (Padmanabhan 1993; Peacock 1998) is able to reproduce precisely the evolution of such regions from small scales (typically  $r \sim 5 h^{-1}$  Mpc) to much larger scales where the dynamics becomes almost linear. However, we explicitly show that neither the Eulerian linear theory nor the Zel’dovich approximation is able to describe their evolution with a sufficient precision. Finally, we show that we are able to reproduce the full matter field surrounding both maxima (build around haloes) and minima (identified to cosmic voids) at  $z = 0$  in numerical simulations.

## 2 COSPHERES IN THE NUMERICAL SIMULATIONS

### 2.1 $N$ -body DEUS simulations

In this work, we use the numerical simulations from the DEUS project. These simulations are publicly available through the ‘Dark Energy Universe Virtual Observatory’ DEUVO Database.<sup>4</sup> They consist of  $N$ -body simulations of Dark Matter (DM) for realistic dark energy models. For more details we refer the interested reader to dedicated sections in Alimi et al. (2010), Rasera et al. (2010), Courtin et al. (2011), Alimi et al. (2012) and Reverdy et al. (2015). These simulations have been realized with an optimized version (Alimi et al. 2012; Reverdy et al. 2015) of the adaptive mesh refinement code RAMSES based on a multigrid Poisson solver (Teyssier 2002; Guillet & Teyssier 2011) for Gaussian initial conditions generated using the Zel’dovich approximation with MPGRAFIC code (Prunet et al. 2008) and input linear power spectrum from CAMB (Lewis, Challinor & Lasenby 2000).

In this paper, we focus only on the flat  $\Lambda$  Cold Dark Matter ( $\Lambda$ CDM) model with cosmological parameters calibrated against measurements of WMAP 5-yr data (Komatsu et al. 2009) and luminosity distances to supernova Type Ia from the UNION data set (Kowalski et al. 2008). The reduced Hubble constant is set to  $h = 0.72$  and the cosmological parameters are  $\Omega_{DE} = 0.74$ ,  $\Omega_b = 0.044$ ,  $n_s = 0.963$  and  $\sigma_8 = 0.79$ . In this paper, we used mainly two different simulations whose properties are summarized in Table 1.

<sup>2</sup> We discuss this term more precisely in this paper.

<sup>3</sup> More generally, for any random position in the density field.

<sup>4</sup> <http://www.deus-consortium.org/deus-data/>

**Table 1.** Simulations used in this paper.  $m_p$  is the mass of each particle while  $M_h$  corresponds to the average mass of the DM haloes selected for stacking. Each simulation is defined by its box size  $L$  in  $h^{-1}$  Mpc and the number of DM particles  $n$ . The simulation in bold is the reference simulation.

	$L = 648, n = 1024^3$	<b><math>L = 2592, n = 2048^3</math></b>	$L = 5184, n = 2048^3$
$m_p$ in $h^{-1} M_\odot$	$\sim 1.8 \times 10^{10}$	<b><math>\sim 1.5 \times 10^{11}</math></b>	$\sim 1.2 \times 10^{12}$
$M_h$ in $h^{-1} M_\odot$	$\sim 4.0 \times 10^{12}$	<b><math>\sim 3.0 \times 10^{13}</math></b>	$\sim 2.5 \times 10^{14}$

If not specified, the numerical simulation used is the reference one defined with  $L_{\text{box}} = 2592 h^{-1} \text{Mpc}$  and  $n_{\text{part}} = 2048^3$  to get both a large volume and a good mass resolution (see Table 1).

## 2.2 Defining CoSpheres

### 2.2.1 Method and definition

We construct CoSpheres in numerical simulation from the position of local extrema in the density field. For central maxima and for  $z = 0$ , we decide to identify these positions with the centre of mass of DM haloes.<sup>5</sup> Such procedure is motivated by the possibility to extend it for observational data where DM haloes could be identified with galaxy, galaxy group or galaxy cluster.

In the symmetric case of a central minima, the position is computed as local minima in the density field smoothed with a Gaussian kernel. In the reference simulation, the physical size of the original coarse grid cell is  $L_{\text{grid}} = 1.26 h^{-1} \text{Mpc}$  before any refinement and we choose a smoothing scale of  $5 h^{-1} \text{Mpc}$ . The comparison with analytical predictions requires to smooth the matter power spectrum on the same scale.

Around each extremum of the density field, we compute the concentric mass by counting the number of particles in the sphere of radius  $r$ , thus imposing the spherical symmetry

$$m(r) = \sum_i m_p \Theta[r - |\mathbf{x}_0 - \mathbf{x}_i|], \quad (2)$$

where  $m_p$  is the mass of each individual particle,  $\mathbf{x}_0$  the position of the extremum and  $\mathbf{x}_i$  the position of the  $i$ th particle.  $\Theta(x)$  is the standard Heaviside function such as  $\Theta(x) = 1$  for  $x > 0$  and 0 elsewhere. From this mass profile we define the mass contrast profile  $\Delta(r)$  defined in equation (1). Note that the density contrast is linked to the mass contrast by

$$\delta(r) = \frac{1}{3} \frac{\partial \Delta}{\partial \log r} + \Delta(r). \quad (3)$$

We now focus on the compensation property. A volume  $V$  is said to be compensated if it satisfies the condition

$$\int_V \rho_m(\mathbf{x}) d^3 \mathbf{x} = \bar{\rho}_m V. \quad (4)$$

The spherical symmetry imposes that the field is compensated in a sphere of radius  $R_1$  if it satisfies

$$m(R_1) = \frac{4\pi}{3} \bar{\rho}_m R_1^3 \Leftrightarrow \Delta(R_1) = 0, \quad (5)$$

this last equation defines the compensation scale  $R_1$  as the *first* radius satisfying  $\Delta(R_1) = 0$ . We stress that this scale is much larger than the typical scale associated with haloes such as the virialization radius  $R_{\text{vir}}$  or  $r_{200}$  such as  $\rho(r_{200}) = 200 \times \bar{\rho}_m$  (Ricotti, Pontzen &

<sup>5</sup> Detected by using a Friend-Of-Friend algorithm with a linking length  $b = 0.2$ .

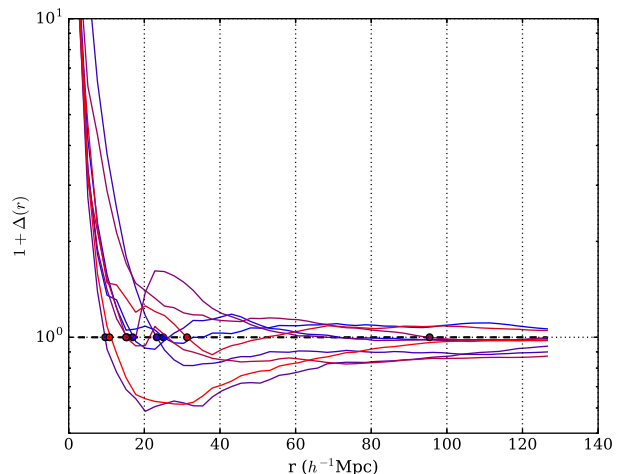


**Figure 1.** Mass contrast profile built around various haloes of mass  $M_h \sim 3 \times 10^{13} h^{-1} M_\odot$  from the reference simulation at  $z = 0$  (see Table 1). For each profile we show the compensation radius  $R_1$  defined by equation (5) and marked with a coloured dot. The majority of profiles are compensated on scale between 10 and 30  $h^{-1} \text{Mpc}$ . We also show a profile with a very large compensation radius  $R_1 \sim 100$ . For central minima, i.e. cosmic voids we obtain similar profiles with finite compensation radii, but in this case, both  $\delta(r)$  and  $\Delta(r)$  are bounded to  $-1$ .

Viel 2007). It is important to note that the compensation radius is defined uniquely for each structure despite the fact that the mass contrast may vanish at other radii  $R_i > R_1$ . For each central extremum, there is a – possibly infinite – number of radii satisfying  $\Delta(R_i) = 0$ ; the compensation radius is defined as the smallest one. Moreover, since these regions must be compensated on the size of the Universe (no mass excess), we have also  $\lim_{r \rightarrow \infty} r^3 \Delta(r) \rightarrow 0$ . In Fig. 1, we show various mass contrast profiles  $1 + \Delta(r)$  centred on DM haloes at  $z = 0$ . For each profile we identify  $R_1$  where the mass is exactly balanced.

We note that compensation radii are always much smaller than the size of the computing box. In the reference simulation, 70 per cent of profiles are compensated on  $R_1 \leq 50 h^{-1} \text{Mpc}$  whereas less than 7 per cent of the profiles have  $R_1 \geq 100 h^{-1} \text{Mpc}$ . It means that the compensation radius could be also measurable on observational data with a sufficiently large volume survey. Moreover,  $R_1$  is roughly of the same order of the effective size  $R_{\text{eff}}$  used in the study of cosmic voids (Platen, Weygaert & Jones 2007; Neyrinck 2008).

### 2.2.2 Average profile at $z = 0$ and stacking procedure

Every compensated region detected in numerical simulation is characterized by two distinct properties. One concerning the central extremum fully described by its height (i.e. the mass of the halo for a maxima and the central  $\delta(\mathbf{x}_0)$  for minima). The second concerning its cosmic environment, characterized by  $R_1$ . Numerical simulation provides an ensemble of profiles with various heights and radii.

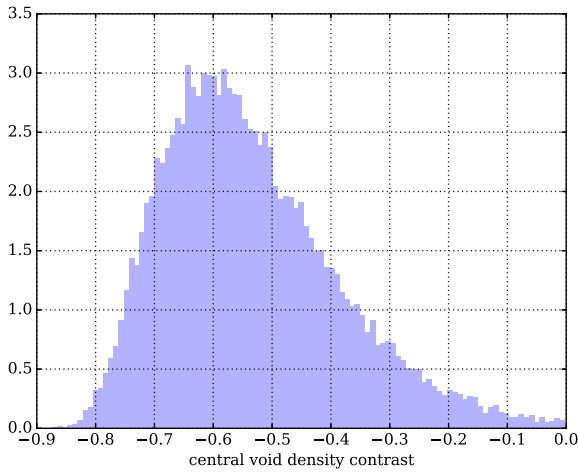


**Figure 2.** Distribution of the central density contrast  $\delta(x_0)$  of 50 000 voids at  $z = 0$  in the reference simulation.

Due to the stochastic nature of the density field, the only physically relevant elements are obtained by computing average quantities and their dispersion. This leads to defined average spherical profiles. All along this paper, average profiles and their corresponding dispersion are built from at least 3000 single profiles. This number ensures a fair statistical estimation. These profiles are built by stacking together CoSpheres with the same height<sup>6</sup> and the same compensation radius  $R_1 \pm dR_1$  where the radial width is  $dR_1 = 1.25 h^{-1} \text{ Mpc}$ . This radial bin is kept constant for the whole paper. For central minima detected in the smoothed density field (see Section 2.2.1), we stack together profiles with the same  $R_1 \pm dR_1$  without density criteria except  $\delta(x_0) < 0$ . In Fig. 2, we plot the distribution of their central density contrasts (whatever  $R_1$ ). We observe that more than 99 per cent of central contrasts are lower  $-0.1$ , beyond Poissonian fluctuations. The resulting profiles are thus averaged over all possible realization of the field with a fixed compensation radius.

In Fig. 3, we show average profiles in the reference simulation at  $z = 0$  from both halo and void with a given compensation radius  $R_1 = 40 h^{-1} \text{ Mpc}$ . In both cases, we show the various radii:

(i) The density radius  $r_1$  such that  $\delta(r_1) = 0$  (in this figure we have  $r_1 \simeq 30 h^{-1} \text{ Mpc}$ ). It separates the over- and underdense areas.

(ii) The compensation radius  $R_1$ . Note that by construction it satisfies  $R_1 \geq r_1$  since it encloses an over- and a underdense shell (such that they compensated each other).

Error bars are computed as the standard error on the mean, i.e.  $\sigma/\sqrt{n}$  where  $\sigma$  is the dispersion and  $n$  the number of profiles considered.

In Fig. 4, we plot the stacked average profiles for various compensation radii  $R_1$  with the same central extrema. Varying  $R_1$  probes the same peak in various cosmic environments. Using these profiles we can study the simple linear scaling assumption. For the mass contrast for example, there could exist  $\Delta_{\text{univ}}(r)$  such that for any  $R_1$  we would have  $\Delta(r, R_1) = \alpha \Delta_{\text{univ}}(\beta r)$ . In Fig. 5, we plot the rescaled profiles  $\Delta(r/R_1)/\Delta_{\text{max}}$  where  $\Delta_{\text{max}}$  is the maximum of the mass contrast. This figure does not indicate any simple linear scaling. Despite being normalized to the same maximal amplitude, the profiles are clearly separated on small scales (for  $r \leq R_1$ ) but

also on larger scales. Furthermore, the position of the maximum changes while varying  $R_1$ , indicating that  $R_{\text{max}} \propto R_1$ . This shows that it is necessary to study the shape of these regions for various compensation radii.

We must also ensure that modifying the simulation parameters do not affect the profiles. A numerical simulation is characterized by a mass and a spatial resolution (see Table 1). Since CoSpheres trace the matter distribution on large or intermediate scales (compared to the coarse grid size), average stacked matter profile result from the dynamics computed on the coarse grid without any refinement. As long as we consider scales larger than a few cells we should not observe any significant deviations for large-scale field when changing the simulation parameters. In other words, the properties of CoSpheres are robust with respect to the resolution parameters of the simulation used to trace the matter field. We illustrate this point on Fig. 6 where we plot the stacked average profile for different numerical simulations but the same halo mass  $M_h = 3.0 \pm 0.075 \times 10^{13} h^{-1} M_\odot$  ( $200 \pm 5$  particles per halo) and three different compensation radii  $R_1$ . For each  $R_1$ , matter profiles are indeed merged together.

### 2.2.3 The spherically compensated cosmic regions at higher redshift

CoSpheres are detected in numerical simulation at  $z = 0$ . We then follow backward in time the evolution of the matter field of such regions using our numerical simulations. For each halo, the position of its progenitor is estimated from the centre of mass of its particles at  $z = 0$ . This estimation is correct since scales probed here are much larger than the halo size (in Appendix A we show how it is possible to model a shift in the theoretical profile). For voids, i.e. central minimum, we assume that its comoving position is conserved during evolution and equals to the position measured at  $z = 0$ . For every redshift and profile, this primordial position is used to compute the spherical mass by counting the number of particles in concentric shells as discussed in Section 2.2.1.

Fig. 7 shows the evolution of profiles with redshift from  $z \simeq 56$  to  $z = 0$  and for both maxima (see Fig. 7a) and minima (see Fig. 7b). This figure illustrates two main points. First, at any redshift, the profile shows the same shape on all scales; an internal over (resp. under) massive core surrounded by its under (resp. over) massive belt. Secondly, the compensation radius (marked with a red dot at  $z = 0$ ) seems to be also conserved in comoving coordinates ( $x$ -axis in comoving  $h^{-1} \text{ Mpc}$ ). This last property will be discussed later in this paper.

This indicates that CoSpheres are generated within the primordial density field at high redshift and are not generated through gravitational dynamics only. In Fig. 8, we thus show – average – CoSphere profiles for different  $R_1$  at a very high redshift  $z \sim 57$  in the simulation. This figure shows that these structures are originated by large-scale primordial density fluctuations with the same compensation properties. In the two following sections, we will study these structures within the primordial field in the framework of GRF (see Section 3). The gravitational evolution of these initial profiles will be studied in Section 4.

## 3 ORIGIN OF COSPHERES IN GAUSSIAN RANDOM FIELD

In this section, we derive the average density profile around extrema in a GRF constrained by the compensation property equation (5).

<sup>6</sup> The same halo mass for maxima.



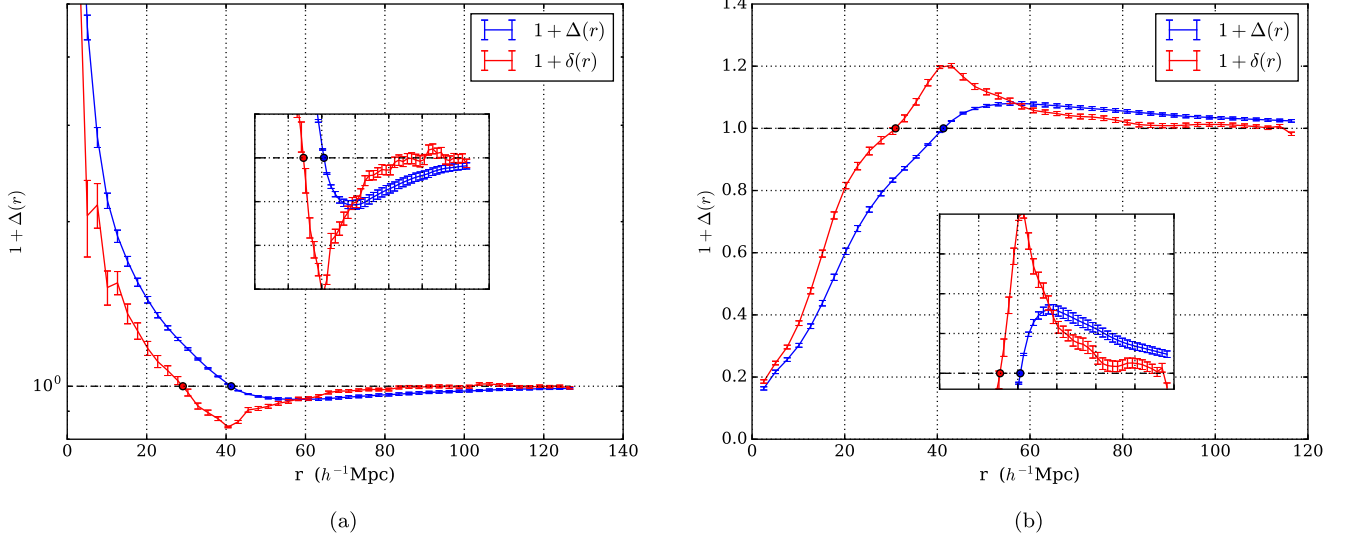


**Figure 3.** Average mass and density contrasts. The blue line represents the mass contrast  $\Delta(r)$  while the red line represents the density contrast  $\delta(r)$ . The density radius (red dot at  $r_1 \sim 27 h^{-1}$  Mpc) and the mass radius (blue square at  $r = 40 h^{-1}$  Mpc) can be clearly identified. On both panels, we plot a zoom of profiles around the compensation radius. (a) Stacked average profile measured around haloes of mass  $M_h \sim 3.0 \times 10^{13} h^{-1}$  Mpc at  $z = 0$  in the reference simulation. We clearly identify the central overdense core until  $r_1$  (red dot) surrounded by the *compensation belt* from  $r = r_1$ . The same occurs for the mass contrast profile (in blue), i.e. an overmassive core for  $r \leq R_1$  (blue square) enclosed in a large undermassive region. (b) Same as panel (a) for central minima. Now the interior region  $r < R_1$  is undermassive while the exterior region is overmassive. The compensation radius has been chosen with the same value than in panel (a).

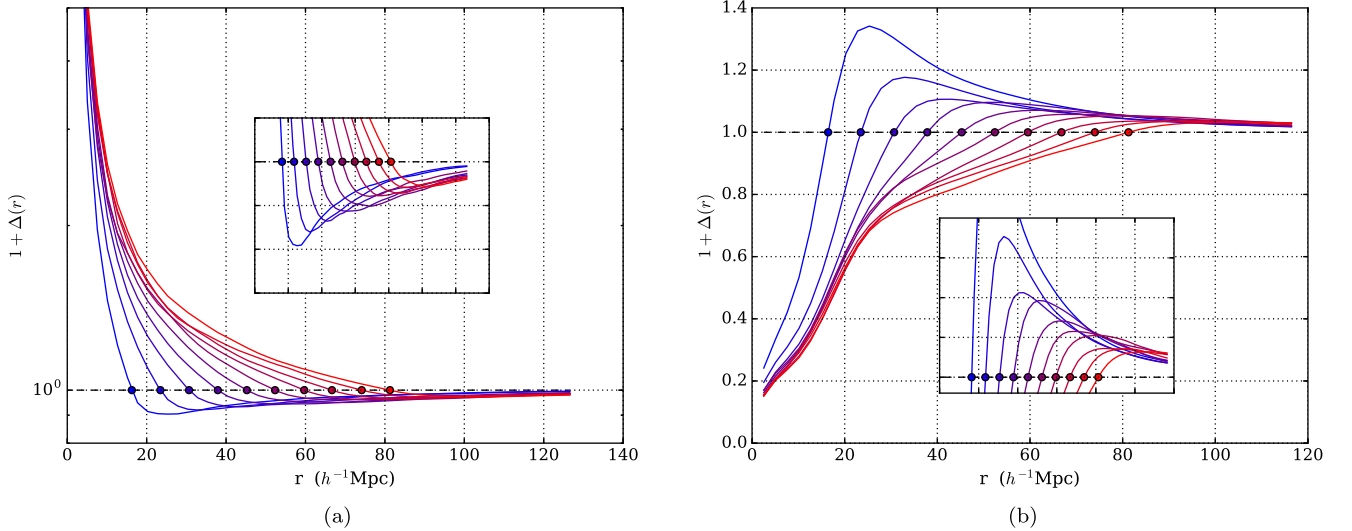


**Figure 4.** Radial average mass contrast profiles at  $z = 0$ . Each curve corresponds to a fixed compensation scale from 15 to 80  $h^{-1}$  Mpc. We do not show the error bars on this figure since they are almost indistinguishable from the curve itself. In both cases we note that small  $R_1$  are associated with strongly contrasted regions. (a) Stacked average profiles around haloes with a mass  $M_h \sim 3.0 \times 10^{13} h^{-1}$  Mpc at  $z = 0$  in the reference simulation. (b) Same as in panel (a) for central underdense regions, i.e. cosmic voids.

Density and mass profiles of CoSpheres are characterized by two family of parameters: the peaks parameters as defined by Bardeen et al. (1986) qualifying the central extrema and the environment parameters.

As was studied in Bardeen et al. (1986), a local extrema at some position  $\mathbf{x}_0$  in GRF can be parametrized by 10 independent – but correlated – parameters. A scalar  $\nu$  quantifying the central height of the extrema

$$\delta(\mathbf{x}_0) = \nu \sigma_0, \quad (6)$$

expressed in units of the fluctuation level  $\sigma_0$

$$\sigma_0 = \left[ \frac{1}{2\pi^2} \int_0^\infty k^2 P(k) dk \right]^{1/2}, \quad (7)$$

where  $P(k)$  is the linear matter power spectrum evaluated at some fixed time  $t_i$  where the field can be assumed to be Gaussian (deep inside the matter-dominated era). The extremum condition imposes that the local gradient of the field  $\eta$  vanishes identically, i.e.

$$\eta_i = \frac{\partial \delta(\mathbf{x}_0)}{\partial x_i} = 0. \quad (8)$$

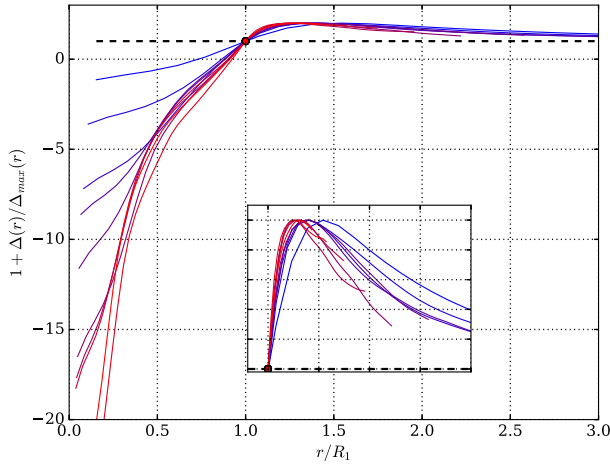


**Figure 5.** Normalized mass contrast profile  $\Delta(r/R_1)/\Delta_{\max}$  (where  $\Delta_{\max}$  is the maximum of each profile) for cosmic voids at  $z = 0$ . We plot the same regions than in Fig. 4(b), with  $R_1$  from 15 to 80  $h^{-1}$  Mpc (red curve). The clear separation between various profiles shows the explicit non-linear dependence of both shape and amplitude in term of  $R_1$  and rules out a simple linear scaling of such radial profiles.

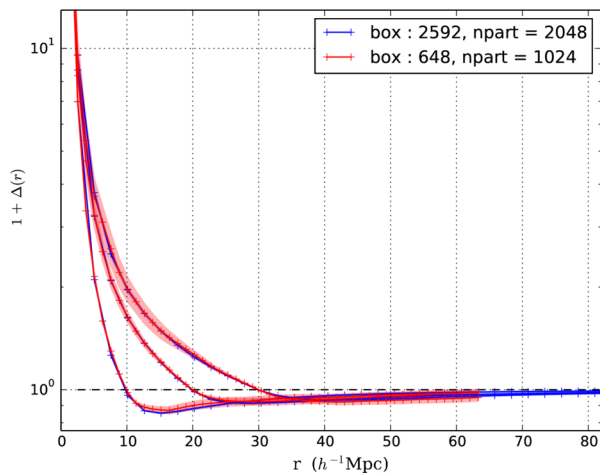


**Figure 6.** Mass contrast profiles  $\Delta(r) + 1$  for three different  $R_1$  and for two different  $\Lambda$ CDM simulations using haloes with the same mass  $M_h \sim 1.5 \times 10^{13} h^{-1} M_\odot$  at  $z = 0$ . The shaded regions show the very low dispersion due to the respective stacking in each simulation. Whatever the simulation, mass contrast profile are superposed for the same compensation radius  $R_1$  and the same halo mass.

The local curvature around the extremum is described by its Hessian matrix  $\zeta$

$$\zeta_{ij} = \frac{\partial^2 \delta(\mathbf{x}_0)}{\partial x_i \partial x_j}. \quad (9)$$

Each eigenvalue of the Hessian matrix must be negative in the case of a central maximum and positive in the opposite case of a minimum (underdense).

Let us now consider the environment parameters. The neighbourhood of the peak is here described by the compensation radius (see equation 5). However, providing this radius only is not sufficient to reconstruct the large variety of profiles and it is necessary to add the compensation density contrast defined on the sphere of radius  $R_1$ . By construction it must be of opposite sign of the central

density contrast. The compensation density  $\delta_1$  is thus defined once averaging over angles the density on the sphere of radius  $r = R_1$

$$\delta(R_1) := \delta_1 = v_1 \sigma_0, \quad (10)$$

with  $v_1/v < 0$ . Without any assumption on the symmetry, we thus need 12 independent parameters : the scalar  $v$ , three components of the  $\eta$  vector, six independent coefficients of the  $\zeta$  matrix (which is real and symmetric) together with  $R_1$  and the reduced compensation density  $v_1$ . In the following, we are going to compute the expected averaged profile in the primordial Gaussian field satisfying both the peak constraints equations (6), (8) and (9) and the environmental constraints equations (5) and (10).

### 3.1 Peaks in GRF

Let us recall the basic elements necessary for the derivation of average quantities in the context of GRF. Our Gaussian field is assumed to be an homogeneous and isotropic random field with zeros mean. We also restrict ourselves to GRF whose statistical properties are fully determined by its power-spectrum (or spectral density)  $P(k)$  i.e. the Fourier transform of the autocorrelation function of the field,  $\xi(r) = \xi(|\mathbf{x}_1 - \mathbf{x}_2|) = \langle \delta(\mathbf{x}_1) \delta(\mathbf{x}_2) \rangle$  :

$$\xi(r) = \frac{1}{2\pi^2} \int_0^\infty k^2 P(k) \frac{\sin(kr)}{kr} dk. \quad (11)$$

The Gaussianity of the field  $\delta(\mathbf{x})$  appears in the computation of the joint probability

$$d\mathcal{P}_N = P[\delta(\mathbf{x}_1), \dots, \delta(\mathbf{x}_N)] d\delta(\mathbf{x}_1) \dots d\delta(\mathbf{x}_N) \quad (12)$$

that the field has values in the range  $[\delta(\mathbf{x}_i), \delta(\mathbf{x}_i) + d\delta(\mathbf{x}_i)]$  for each position  $\mathbf{x}_i$ . In this particular case of homogeneous and isotropic GRF, this probability reaches

$$d\mathcal{P}_N = \frac{1}{\sqrt{(2\pi)^N \det \mathbf{M}}} \exp \left[ -\frac{1}{2} \delta^t \cdot \mathbf{M}^{-1} \cdot \delta \right] \prod_{i=1}^N d\delta_i, \quad (13)$$

where  $\delta$  is the  $N$  dimensional vector  $\delta_i = \delta(\mathbf{x}_i)$  and  $\mathbf{M}$  is the  $N \times N$  covariance matrix, here fully determined by the field autocorrelation

$$M_{ij} := \langle \delta_i \delta_j \rangle = \xi(|\mathbf{x}_i - \mathbf{x}_j|), \quad (14)$$

where the average operator  $\langle \dots \rangle$  denotes hereafter an ensemble average. The ergodic assumption identifies the ensemble average  $\langle \dots \rangle$  computed on all possible statistical realization of the observable to its spatial averaging, i.e. its mean over a sufficiently large volume. The average of any operator  $X$  can be written as a mean over its Fourier component  $\tilde{X}$

$$\langle X \rangle := \frac{1}{2\pi^2 \sigma_0^2} \int_0^\infty k^2 P(k) \tilde{X}(k) dk = \frac{\int_0^\infty k^2 P(k) \tilde{X}(k) dk}{\int_0^\infty k^2 P(k) dk}. \quad (15)$$

Furthermore, we are interested in deriving the properties of the field subject to  $n$  linear constraints  $C_1, \dots, C_n$ . Following Bertschinger (1987), we write each constraint  $C_i$  as a convolution of the field

$$C_i[\delta] := \int W_i(\mathbf{x}_i - \mathbf{x}) \delta(\mathbf{x}) d\mathbf{x} = c_i, \quad (16)$$

where  $W_i$  is the corresponding window function and  $c_i$  is the value of the constraint. For example, constraining the value of the field to a certain  $\delta_0$  at some point  $\mathbf{x}_0$  leads to  $W_i = \delta_D(\mathbf{x} - \mathbf{x}_0)$  and  $c_i = \delta_0$ . Since the constraints are linear, their statistics is also Gaussian and

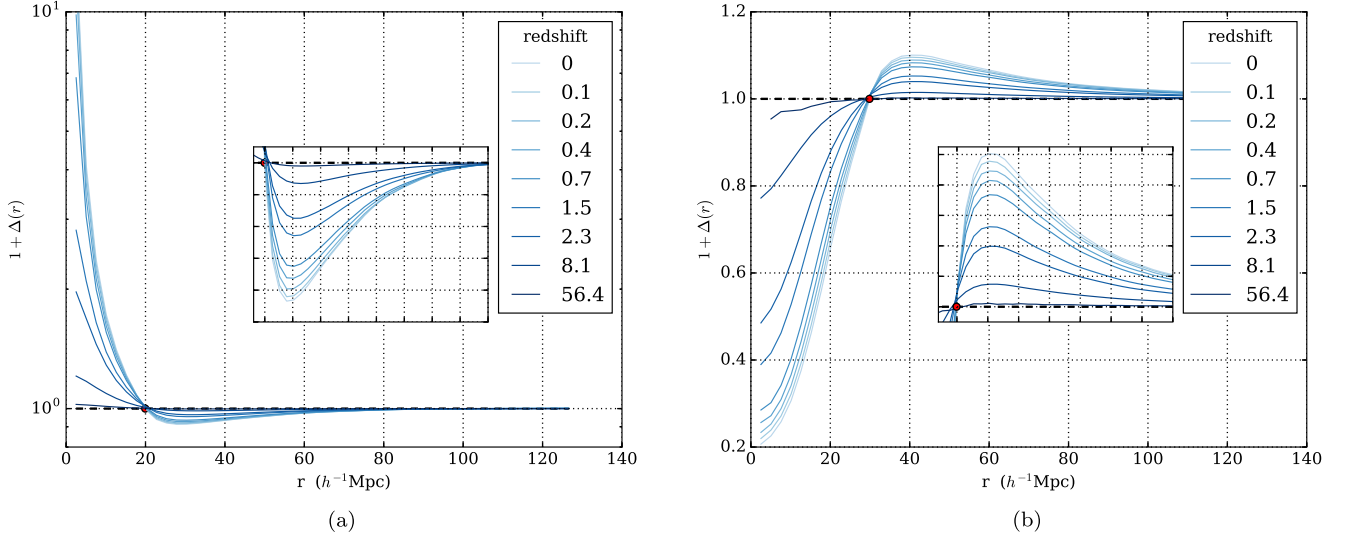


**Figure 7.** Evolution of the mass contrast profile for both maxima and minima in the density field. The radial scale is in comoving  $h^{-1}$  Mpc and each curve corresponds to a single redshift. (a) Mass contrast profile for  $R_1 = 20 h^{-1}$  Mpc for various redshift from an halo with a mass  $M_h = 3 \times 10^{13} h^{-1} M_\odot$ . It is computed by stacking together single profiles computed from the progenitor of each halo registered at  $z = 0$ . As discussed in Section 2.2.3, the position of the progenitor at any  $z$  is estimated from the centre of mass of the particles composing the halo at  $z = 0$ . (b) Same as in panel (a) but centred on local minima and for  $R_1 = 30 h^{-1}$  Mpc. For tracing backward in time the evolution of such regions, we simply assumed that the comoving positions of central minima detected at  $z = 0$ , is conserved during the whole evolution. Such estimation provides satisfying results.

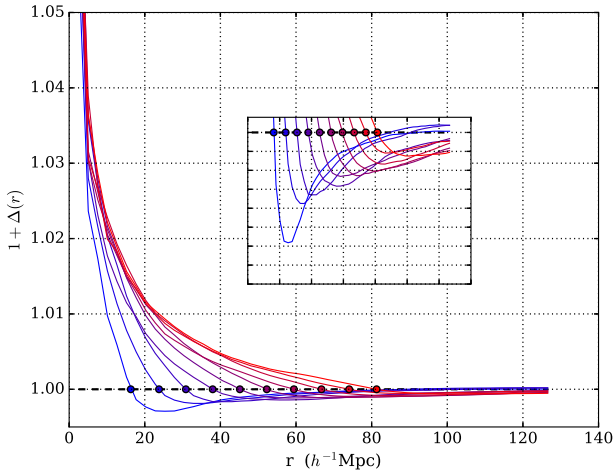


**Figure 8.** Mass contrast profiles at high redshift  $z \simeq 57$  for different  $R_1$  between 15 and  $80 h^{-1}$  Mpc detected originally from haloes with the same mass  $M_h = 3.0 \times 10^{13} h^{-1} M_\odot$ .

the joint probability  $d\mathcal{P}[\mathbf{C}]$  that the field satisfies these conditions is (van de Weygaert & Bertschinger 1996; Bertschinger 1987)

$$d\mathcal{P}[\mathbf{C}] = \frac{1}{\sqrt{(2\pi)^n \det \mathbf{Q}}} \exp \left[ -\frac{1}{2} \mathbf{C}^t \cdot \mathbf{Q}^{-1} \cdot \mathbf{C} \right] \prod_{i=1}^n dc_i, \quad (17)$$

where  $\mathbf{Q}$  is the covariance matrix of the constraints  $\mathbf{C} = \{C_1, \dots, C_n\}$  defined as  $\mathbf{Q} = \langle \mathbf{C}^t \cdot \mathbf{C} \rangle$ . The average density profile  $\langle \delta \rangle$  subject to  $\mathbf{C}$  is computed as the most probable profile given  $\mathbf{C}$  and reaches

$$\langle \delta \rangle(\mathbf{x}) := \langle \delta | \mathbf{C} \rangle(\mathbf{x}) = \xi_i(\mathbf{x}) Q_{ij}^{-1} c_j, \quad (18)$$

where  $\xi_i(\mathbf{x})$  is the correlation function between the field and the  $i$ th constraint

$$\xi_i(\mathbf{x}) = \langle \delta(\mathbf{x}) C_i \rangle, \quad (19)$$

and  $Q_{ij}$  is the  $(ij)$  element of the correlation matrix  $\mathbf{Q}$ . Bardeen et al. (1986) derived the average spherical<sup>7</sup> density profile of peaks in GRF in term of the reduced height  $\nu$  (see equation 6), its autocorrelation function  $\xi(r)$  (see equation 11) and the curvature parameter  $x$  defined by

$$x = -\frac{3}{\sigma_0 \sqrt{\langle k^4 \rangle}} \frac{\partial^2 \delta(\mathbf{x}_0)}{\partial r^2}. \quad (20)$$

It yields

$$\langle \delta \rangle_{\text{peaks}}(r) = \frac{\nu - \gamma x}{1 - \gamma^2} \frac{\xi(r)}{\sigma_0} + \frac{\nu - x/\gamma}{1 - \gamma^2} \frac{R_*^2}{3} \frac{\Delta \xi(r)}{\sigma_0}, \quad (21)$$

with  $R_* = \sqrt{3 \langle k^2 \rangle / \langle k^4 \rangle}$  and  $\gamma = \langle k^2 \rangle / \sqrt{\langle k^4 \rangle}$ . The various moments of  $k$  are given by

$$\langle k^n \rangle := \frac{1}{2\pi^2 \sigma_0^2} \int_0^\infty k^{2+n} P(k) dk. \quad (22)$$

In the next section, we extend this result by implementing the compensation conditions equations (5) and (10).

### 3.2 CoSpheres in Gaussian random fields

In the following, we use several functions involving  $r$  and  $R_1$ . In order to simplify the notations, we note the Fourier components as

$$W_r := 3 \frac{\sin(kr) - kr \cos(kr)}{(kr)^3}, \quad (23)$$

$$J_r := \frac{\sin(kr)}{kr}, \quad (24)$$

which are respectively the Fourier transform of the top-hat and the delta functions. Note that they are linked to the spherical Bessel

<sup>7</sup> Their calculation goes beyond the spherical approximation but we restrict here to the simplest spherical case obtained by averaging over angles.



functions as  $W_r = 3/(kr)j_1(kr)$  and  $J_r = j_0(kr)$ . We also denote with the ‘1’ subscript these quantities evaluated at the particular radius  $r = R_1$ , i.e.

$$W_1 := W_r|_{r=R_1}, \quad (25)$$

$$J_1 := J_r|_{r=R_1}. \quad (26)$$

### 3.2.1 The average density profile of CoSphere

We now derive the average matter profile being both

(i) centred on an extremum, i.e. satisfying the conditions equations (6), (8) and (9), and

(ii) compensated on a finite scale  $R_1$ . This is implemented by the compensation constraints equations (5) and (10).

The spherical peak constraints are (see equation 16)

$$C_v[\delta] := \int \delta_D[\mathbf{x} - \mathbf{x}_0] \delta(\mathbf{x}) d\mathbf{x} = c_v \equiv \sigma_0 \nu, \quad (27)$$

$$C_{\eta_i}[\delta] := \int \partial_i \delta_D[\mathbf{x} - \mathbf{x}_0] \delta(\mathbf{x}) d\mathbf{x} = c_{\eta_i} \equiv 0, \quad (28)$$

$$C_x[\delta] := \int \frac{\partial^2}{\partial \mathbf{x}^2} \delta_D[\mathbf{x} - \mathbf{x}_0] \delta(\mathbf{x}) d\mathbf{x} = c_x \equiv -\sigma_0 \frac{x \sqrt{\langle k^4 \rangle}}{3}, \quad (29)$$

where  $\delta_D$  is the usual Dirac function. On the other hand, the *environmental* constraints (see equations 5 and 10) can be written

$$C_{R_1}[\delta] := \int \Theta[R_1 - |\mathbf{x} - \mathbf{x}_0|] \delta(\mathbf{x}) d\mathbf{x} = c_{R_1} \equiv 0, \quad (30)$$

$$C_{v_1}[\delta] := \int \delta_D[R_1 - |\mathbf{x} - \mathbf{x}_0|] \delta(\mathbf{x}) d\mathbf{x} = c_{v_1} \equiv \sigma_0 \nu_1, \quad (31)$$

where  $\Theta$  is the Heaviside step function.  $\nu_1$  must also satisfy equation (10) and thus satisfy  $\nu_1/\nu < 0$ . Note that in equation (30), the constraint value is  $c_{R_1} = 0$  and only three eigenvalues for the constraints are non-zero:  $\nu$ ,  $x$  and  $\nu_1$ . The original peak constraints involve the correlations

$$\xi_v(r) := \langle \delta(\mathbf{x}) C_v \rangle = \sigma_0^2 \langle J_r \rangle, \quad (32)$$

$$\xi_x(r) := \langle \delta(\mathbf{x}) C_x \rangle = -\sigma_0^2 \langle k^2 J_r \rangle. \quad (33)$$

The compensation constraints introduce new correlations in the computation of the average profile

$$\xi_{R_1}(r) := \langle \delta(\mathbf{x}) C_{R_1} \rangle = \sigma_0^2 \langle W_1 J_r \rangle, \quad (34)$$

$$\xi_{v_1}(r) := \langle \delta(\mathbf{x}) C_{v_1} \rangle = \sigma_0^2 \langle J_1 J_r \rangle. \quad (35)$$

Using equation (18), the average profiles are linear in  $\nu$ ,  $x$  and  $\nu_1$  while  $R_1$  implicitly appears in the various radial functions, such that we can write

$$\langle \delta \rangle(r) = \sigma_0 (\nu \delta_\nu(r) + x \delta_x(r) + \nu_1 \delta_{v_1}(r)) \quad (36)$$

where  $\delta_\alpha$  with  $\alpha = \{\nu, x, \nu_1\}$  are functions of  $r$  and  $R_1$  only. By construction, each  $\delta_\alpha(r)$  must satisfy the compensation property, i.e. its integral must vanish at  $r = R_1$

$$\int_0^{R_1} u^2 \delta_\alpha(u) du = 0. \quad (37)$$

From equation (18), we know that each  $\delta_\alpha(r)$  is a linear combination of the four functions  $\xi_\alpha(r)$  (see equations 32–35). To simplify the notations, we define three intermediate functions build from the  $\xi_\alpha$  functions and satisfying the condition equation (37)

$$f_0(r) = \frac{\langle k^2 W_1 \rangle \langle J_r \rangle - \langle W_1 \rangle \langle k^2 J_r \rangle}{\langle k^2 W_1 \rangle - \langle k^2 \rangle \langle W_1 \rangle}, \quad (38)$$

$$f_1(r) = \frac{\langle W_1 J_r \rangle \langle k^2 W_1 \rangle - \langle W_1^2 \rangle \langle k^2 J_r \rangle}{\langle W_1 \rangle \langle k^2 W_1 \rangle - \langle k^2 \rangle \langle W_1^2 \rangle}, \quad (39)$$

$$f_2(r) = \frac{\langle J_1 J_r \rangle \langle k^2 W_1 \rangle - \langle J_1 W_1 \rangle \langle k^2 J_r \rangle}{\langle J_1 \rangle \langle k^2 W_1 \rangle - \langle k^2 \rangle \langle J_1 W_1 \rangle}, \quad (40)$$

these functions have also been normalized such that  $f_i(0) = 1$ . Each  $\delta_\alpha(r)$  is then a linear combination of these three functions. Note that  $f_i(R_1) \neq 0$ . We also introduce three parameters  $\lambda_i$  defined locally around the extremum

$$\lambda_i := -3 \frac{\partial^2 f_i}{\partial r^2} \quad \text{for } r \rightarrow 0. \quad (41)$$

They explicitly reach

$$\lambda_0 = \frac{\langle k^2 W_1 \rangle \langle k^2 \rangle - \langle W_1 \rangle \langle k^4 \rangle}{\langle k^2 W_1 \rangle - \langle k^2 \rangle \langle W_1 \rangle}, \quad (42)$$

$$\lambda_1 = \frac{\langle k^2 W_1 \rangle^2 - \langle W_1^2 \rangle \langle k^4 \rangle}{\langle W_1 \rangle \langle k^2 W_1 \rangle - \langle k^2 \rangle \langle W_1^2 \rangle}, \quad (43)$$

$$\lambda_2 = \frac{\langle k^2 J_1 \rangle \langle k^2 W_1 \rangle - \langle J_1 W_1 \rangle \langle k^4 \rangle}{\langle J_1 \rangle \langle k^2 W_1 \rangle - \langle k^2 \rangle \langle J_1 W_1 \rangle}. \quad (44)$$

With these notations and a bit of algebra, we obtain the  $\delta_\alpha$  functions

$$\begin{aligned} \delta_\nu(r) = & f_0(r) \frac{\lambda_1 f_2^1 - \lambda_2 f_1^1}{\omega} + f_1(r) \frac{\lambda_2 f_0^1 - \lambda_0 f_2^1}{\omega} \\ & + f_2(r) \frac{\lambda_0 f_1^1 - \lambda_1 f_0^1}{\omega} \end{aligned} \quad (45)$$

together with

$$\frac{\delta_x(r)}{\sqrt{\langle k^4 \rangle}} = f_0(r) \frac{f_1^1 - f_2^1}{\omega} + f_1(r) \frac{f_2^1 - f_0^1}{\omega} + f_2(r) \frac{f_0^1 - f_1^1}{\omega} \quad (46)$$

and

$$\delta_{v_1}(r) = f_0(r) \frac{\lambda_2 - \lambda_1}{\omega} + f_1(r) \frac{\lambda_0 - \lambda_2}{\omega} + f_2(r) \frac{\lambda_1 - \lambda_0}{\omega}, \quad (47)$$

where

$$\omega = \lambda_0 (f_1^1 - f_2^1) + \lambda_1 (f_2^1 - f_0^1) + \lambda_2 (f_0^1 - f_1^1), \quad (48)$$

and we used the notation  $f_i^1 := f_i(R_1)$ . Note that  $\lambda_i$  and  $f_i^j$  are not constant but non-linear functions of  $R_1$ .

The  $\delta_\alpha$  functions satisfy the following properties around  $r = 0$

$$\begin{cases} \delta_\nu(r) & \simeq 1 + \mathcal{O}(r^4), \\ \delta_x(r) & \simeq -\sqrt{\langle k^4 \rangle} \frac{r^2}{6} + \mathcal{O}(r^4), \\ \delta_{v_1}(r) & \simeq \mathcal{O}(r^4), \end{cases} \quad (49)$$

while in  $r = R_1$  we have

$$\begin{cases} \delta_\nu(R_1) & = 0, \\ \delta_x(R_1) & = 0, \\ \delta_{v_1}(R_1) & = 1, \end{cases} \quad (50)$$

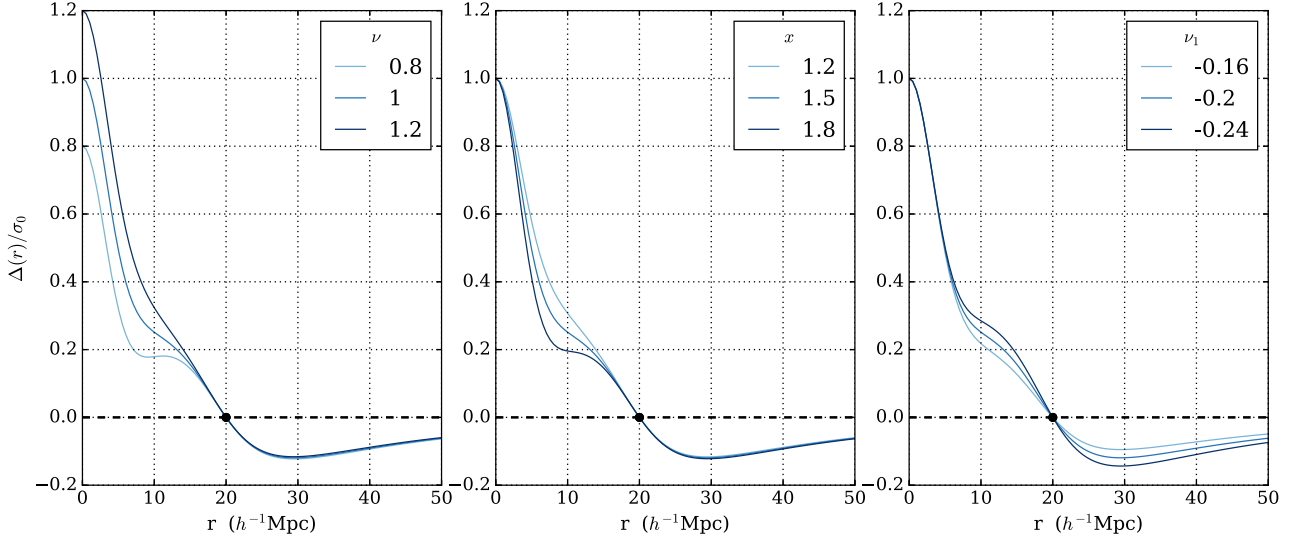


**Figure 9.** Rescaled mass contrast profile  $\langle \Delta(r) \rangle / \sigma_0$  derived in equation (51) for  $R_1 = 20 h^{-1} \text{ Mpc}$  (black dot). On each panel we vary one of the shape parameters  $\nu$ ,  $x$  or  $\nu_1$ . This figure illustrates that the peak parameters  $\nu$  and  $x$  affect the profile on small scales (around the peak) while  $\nu_1$  acts on the large-scale shape of the matter profile. Note that  $\nu_1$  changes the slope of the mass contrast profile around  $R_1$  since by definition  $\Delta'(R_1) = 3/R_1 \sigma_0 \nu_1$ . This analysis is absolutely symmetric for the case of a central underdensity. Note that the elbow around  $r = 10 h^{-1} \text{ Mpc}$  is an artificial feature induced by forcing one shape parameter to vary while fixing the other ones. In practice, these shape parameters are correlated together and this scale does not appear in realistic profiles (see other figures for example). We discuss these correlations in more detail in Alimi & de Fromont (2017a).

ensuring that  $\langle \delta \rangle (R_1) = \sigma_0 \nu_1$ .

### 3.2.2 The averaged mass contrast profile of CoSphere

The average mass contrast profile  $\langle \Delta \rangle (r)$  is obtained by integrating  $\langle \delta \rangle (r)$  with equation (1). By linearity of the mapping  $\delta \leftrightarrow \Delta$ ,  $\langle \Delta \rangle$  takes the same shape than equation (36) where each  $\delta_\alpha(r)$  transforms to  $\Delta_\alpha(r)$ , i.e. we have

$$\langle \Delta \rangle (r) = \sigma_0 (\nu \Delta_\nu(r) + x \Delta_x(r) + \nu_1 \Delta_{\nu_1}(r)) \quad (51)$$

Since each function  $\delta_\alpha$  is a linear combination of the  $f_i$ , the  $\Delta_\alpha$  functions will be linear combinations of the  $F_i$  functions defined as

$$F_i(r) := \frac{3}{r^3} \int_0^r u^2 f_i(u) du. \quad (52)$$

Moreover, the  $f_i$  functions only involve linear combinations of  $J_r = \sin(kr)/(kr)$ . The  $F_i$  are thus obtained from  $f_i$  by the simple replacement  $J_r \rightarrow W_r$ , leading to

$$F_0(r) = \frac{\langle k^2 W_1 \rangle \langle W_r \rangle - \langle W_1 \rangle \langle k^2 W_r \rangle}{\langle k^2 W_1 \rangle - \langle k^2 \rangle \langle W_1 \rangle}, \quad (53)$$

$$F_1(r) = \frac{\langle W_1 W_r \rangle \langle k^2 W_1 \rangle - \langle W_1^2 \rangle \langle k^2 W_r \rangle}{\langle W_1 \rangle \langle k^2 W_1 \rangle - \langle k^2 \rangle \langle W_1^2 \rangle}, \quad (54)$$

$$F_2(r) = \frac{\langle J_1 W_r \rangle \langle k^2 W_1 \rangle - \langle J_1 W_1 \rangle \langle k^2 W_r \rangle}{\langle J_1 \rangle \langle k^2 W_1 \rangle - \langle k^2 \rangle \langle J_1 W_1 \rangle}. \quad (55)$$

We can check that for  $i = \{0, 1, 2\}$  we have  $F_i(R_1) = 0$  ensuring that  $\langle \Delta \rangle (R_1) = 0$  whatever the shape parameters. The mapping between the  $\Delta_\alpha$  functions and the  $F_i$  is given by

$$\begin{aligned} \Delta_\nu(r) = & F_0(r) \frac{\lambda_1 f_2^1 - \lambda_2 f_1^1}{\omega} + F_1(r) \frac{\lambda_2 f_0^1 - \lambda_0 f_2^1}{\omega} \\ & + F_2(r) \frac{\lambda_0 f_1^1 - \lambda_1 f_0^1}{\omega}, \end{aligned} \quad (56)$$

while for  $x$  we have

$$\frac{\Delta_x(r)}{\sqrt{\langle k^4 \rangle}} = F_0(r) \frac{f_1^1 - f_2^1}{\omega} + F_1(r) \frac{f_2^1 - f_0^1}{\omega} + F_2(r) \frac{f_0^1 - f_1^1}{\omega} \quad (57)$$

and

$$\Delta_{\nu_1}(r) = F_0(r) \frac{\lambda_2 - \lambda_1}{\omega} + F_1(r) \frac{\lambda_0 - \lambda_2}{\omega} + F_2(r) \frac{\lambda_1 - \lambda_0}{\omega}. \quad (58)$$

The resulting mass contrast profile satisfies, for  $r \rightarrow 0$

$$\begin{cases} \Delta_\nu(r) \simeq 1 + \mathcal{O}(r^4), \\ \Delta_x(r) \simeq -\sqrt{\langle k^4 \rangle} \frac{r^2}{10} + \mathcal{O}(r^4), \\ \Delta_{\nu_1}(r) \simeq \mathcal{O}(r^4), \end{cases} \quad (59)$$

while in  $r = R_1$  we have, by construction

$$\begin{cases} \Delta_\nu(R_1) = 0, \\ \Delta_x(R_1) = 0, \\ \Delta_{\nu_1}(R_1) = 0, \end{cases} \quad (60)$$

together with

$$\Delta'_{\nu_1}(R_1) = \frac{3}{R_1} \nu_1 \sigma_0, \quad (61)$$

where a prime denotes the derivative with respect to  $r$ . In Fig. 9, we plot the averaged mass contrast equation (51) for  $R_1 = 20 h^{-1} \text{ Mpc}$ . In each panel, we change one of the shape parameters  $\nu$ ,  $x$  and  $\nu_1$  to illustrate their effect. Since both  $\nu$  and  $x$  are associated with the central peak, changing their value only affects the profile on small scales, typically  $r \lesssim R_1/2$ . The compensation density  $\nu_1$  defines the

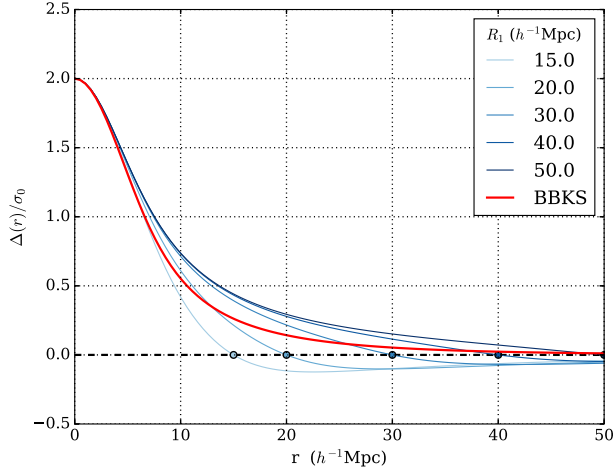


**Figure 10.** Averaged mass contrast profile in the primordial field. Each blue curve corresponds to a CoSphere profile with fixed peak parameters ( $x$  and  $\nu$ ) but various  $R_1$  ( $\nu_1$  is also fixed to an arbitrary value of  $-0.5$ ). The red curve is the corresponding BBKS profile equation (21) with the same peak parameters  $\nu$  and  $x$ . Local matter profile around the extremum are similar while on larger scales our model allow to probe different cosmic environments through  $R_1$  and  $\nu_1$ . Even if it does not appears on the plot, this BBKS profile is also compensated on a larger scale, here  $R_1 \simeq 60 h^{-1}$  Mpc.

structure of the profile on larger scales from  $r \sim R_1$ . This behaviour clearly illustrates that  $x$  and  $\nu$  are defined on the peak while  $R_1$  and  $\nu_1$  qualify the large-scale surrounding environment of the peak.

### 3.2.3 Comparison with the BBKS peak profile

The peak profiles derived by BBKS (see equation 21) describe the large-scale environment surrounding extrema in Gaussian field where we only provide the properties of the density field on the peak. Our calculation is thus an extension of this result including the physical properties of the large-scale environment around the peak.

Our formalism allows to probe different cosmic environment for the same central extremum. This environment is defined through  $R_1$  and the compensation density  $\delta_1 = \nu_1 \sigma_0$ . For the same central peak, we can describe a large variety of cosmic configurations while this region is completely fixed in the standard BBKS approach.

In Fig. 10, we show how it is possible to describe various environments by varying  $R_1$  while keeping constant  $\nu$  and  $x$ , i.e. the central peak. We also plot the BBKS profile, fully determined by  $x$  and  $\nu$ . Small values of  $R_1$  correspond to isolated peaks in large underdense regions while increasing the compensation scale allows to probe denser regions. The exact same symmetric case occurs for cosmic voids with the reimplement  $\nu \rightarrow -\nu$ ,  $x \rightarrow -x$  and  $\nu_1 \rightarrow -\nu_1$ .

The standard BBKS profile can be written as in equation (36) with the corresponding  $\delta_v^p(r)$  (where p stands for ‘peak’)

$$\delta_v^p(r) = \frac{\langle k^4 \rangle \langle J_r \rangle - \langle k^2 \rangle \langle k^2 J_r \rangle}{\langle k^4 \rangle - \langle k^2 \rangle^2}, \quad (62)$$

$$\delta_x^p(r) = -\sqrt{\langle k^4 \rangle} \left[ \frac{\langle k^2 \rangle \langle J_r \rangle - \langle k^2 J_r \rangle}{\langle k^4 \rangle - \langle k^2 \rangle^2} \right], \quad (63)$$

$$\delta_{\nu_1}^p(r) = 0. \quad (64)$$

In the peak profile of BBKS, it is possible to map the peak parameters  $\nu$  and  $x$  to their effective  $R_1$  and  $\nu_1$ . These effective  $R_1$  and  $\nu_1$  satisfy

$$\begin{cases} \lambda_0(R_1) &= \sqrt{\langle k^4 \rangle} x / \nu, \\ \nu_1 &= \nu f_0^1(R_1), \end{cases} \quad (65)$$

where we recall

$$\lambda_0 = \frac{\langle k^2 W_1 \rangle \langle k^2 \rangle - \langle W_1 \rangle \langle k^4 \rangle}{\langle k^2 W_1 \rangle - \langle k^2 \rangle \langle W_1 \rangle}, \quad (66)$$

$$f_0^1 = \frac{\langle k^2 W_1 \rangle \langle J_1 \rangle - \langle W_1 \rangle \langle k^2 J_1 \rangle}{\langle k^2 W_1 \rangle - \langle k^2 \rangle \langle W_1 \rangle}. \quad (67)$$

Note that this effective compensation radius  $R_1$  depends only on the fraction  $x/\nu$ . For each value of  $x/\nu$  it is possible to find a finite compensation radius  $R_1$ .

### 3.3 Numerical reconstruction of CoSpheres in GRF

At very high redshift, the density field follows a Gaussian statistics. This property is inherited from the inflation phase of the young Universe. In the previous sections, we derived the average profiles of spherically compensated inhomogeneities in the framework of GRF. As presented in Section 2.2.3, the simulations can be used to follow backward in time the evolution of CoSpheres detected at  $z=0$ . Using this numerical procedure we can compare our expected Gaussian profiles (see equation 36) with the numerical matter field of compensated peaks at higher redshift.

Each theoretical profile is parametrized by four scalars. The compensation radius  $R_1$  can be read directly from the profile (built at fixed  $R_1$ ). The shape parameters  $\nu$ ,  $x$  and  $\nu_1$  are computed using a standard  $\chi^2$  method defined from the measured profile  $\Delta_j$  and its error  $\sigma_j$  for  $r = r_j$ .

We stress that this reconstruction is done on the mass contrast profile and not directly from the density profile. Indeed, computing the number of particles in concentric spheres leads naturally to the mass contrast while the density must be computed by taking its radial derivative (see equation 3). Moreover, since mass contrast is integrated over  $r$ , its statistical noise is smaller than for  $\delta(r)$ .

At high redshift, we allow a possible shift  $R = |\mathbf{x}_c - \mathbf{x}_0|$  between the true position of the central extrema  $\mathbf{x}_0$  and its estimation  $\mathbf{x}_c$  by adding this degree of freedom in the previous  $\chi^2$  analysis. The effect of such shift of the central position on theoretical profiles is discussed in Appendix A. We show that the analytical profile around a shifted position is modified by an effective smoothing of the linear power spectrum  $P(k) \rightarrow P(k) \text{sinc}(kR)$ .

In Fig. 11, we show a measured mass contrast profile at high redshift (blue curve). We show in red the corresponding expected profile (see Section 3.2.2) whose shape parameters are estimated from the previous  $\chi^2$ . We also show in purple the expected shape from the BBKS profile with best-fitting values for  $x$  and  $\nu$

We observe a high accuracy agreement between our prediction equation (51) and the measured averaged profile on all scales (this fit can be reproduce for any  $R_1$ ). The standard BBKS profile suffers from a lack of degrees of freedom and is not able to reproduce the shape on large scales. The standard peak profile cannot be used to describe the large-scale compensated cosmic regions, hence the CoSphere model.

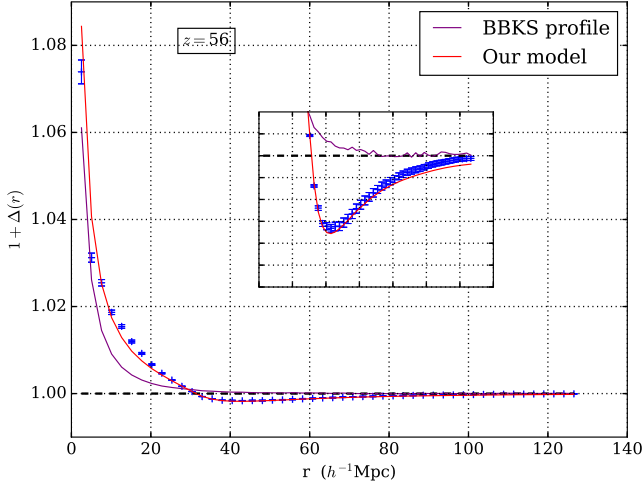


**Figure 11.** Averaged mass contrast profile at high redshift  $z = 56$  in the reference simulation (blue curve). The purple curve is the standard BBKS profile (Bardeen et al. 1986) with  $\nu$  and  $x$  obtained by a standard  $\chi^2$  minimization. The red curve is the CoSphere profile equation (51) whose shape parameters ( $\nu$ ,  $x$  and  $\nu_1$ ) are obtained by the same  $\chi^2$  optimization. We note the excellent agreement between our profile and the measured one while the standard peak formalism fails to reproduce the shape on the matter field.

## 4 DYNAMICAL EVOLUTION OF COSPHERES

In this section, we study the gravitational collapse of CoSpheres resulting from the primordial fluctuations of the matter field as studied in Section 3.

### 4.1 The Lagrangian spherical collapse

Due to the spherical symmetry of our problem, the evolution of the matter profile reduces to the dynamics of concentric shells with fixed mass. This leads to the Lagrangian SC model, first introduced in Gunn & Gott (1972) and largely discussed in Padmanabhan (1993) and Peacock (1998). While it was first developed in the context of Einstein-de-Sitter cosmology, it has been extended to  $\Lambda$ CDM (Lahav et al. 1991) and more general models of DE (Wang & Steinhardt 1998). In this section, we derive a simple formalism for the SC suited to our problem.

As we focus in this paper on the standard  $\Lambda$ CDM model describing a flat Universe ( $K = 0$ ) with collisionless CDM and a cosmological constant  $\Lambda$ , the homogeneous background is described by the Friedman and the Raychaudhuri equations

$$\left(\frac{\dot{a}}{a}\right)^2 = H_0^2 \left[ \frac{\Omega_m^0}{a^3} + 1 - \Omega_m^0 \right], \quad (68)$$

$$\frac{\ddot{a}}{a} = -\frac{H_0^2}{2} \left[ \frac{\Omega_m^0}{a^3} + 2\Omega_m^0 - 2 \right], \quad (69)$$

where a dot (e.g.  $\dot{X}$ ) denotes the derivative with respect to the proper time  $t$ ,  $H_0$  is the Hubble constant today and  $\Omega_m^0 = 8\pi G \bar{\rho}_{m,0}/(3H_0^2)$ . Moreover, in the quasi static limit (QSL) where the time variation of the gravitational potential are smooth, i.e.  $\dot{\Phi} \ll \Phi \dot{a}/a$  and for scales deep inside the Hubble radius  $r \ll 1/(aH)$ , the first-order perturbed equations reduce to the well-known Poisson equation linking the local density contrast  $\delta$  to the Newtonian potential  $\Phi$

$$\nabla^2 \Phi = 4\pi G \bar{\rho}_m \delta. \quad (70)$$

Using the spherical symmetry, the Poisson equation can be integrated once to give the Newtonian acceleration

$$\frac{\partial \Phi}{\partial r} = r \frac{4\pi G \bar{\rho}_m}{3} \Delta(r), \quad (71)$$

with  $\Delta(r)$  is the mass contrast. It thus drives the local gravitational acceleration. Note that for  $r = R_1$  we have  $\nabla \Phi = 0$ . In the QSL, the equation of motion of each shell with a physical radius  $r = a\chi$  is (Peebles 1980)

$$\ddot{r} = \frac{\ddot{a}}{a} r - \nabla \Phi. \quad (72)$$

For each shell we define the dimensionless comoving displacement

$$\mathcal{R}(\chi_i, t) = \frac{\chi(t)}{\chi_i}, \quad (73)$$

where  $\chi(t)$  is the comoving radius of the shell at some time  $t$  and  $\chi$  its initial radius  $\chi_i = \chi(t_i)$ . The equation of motion for each concentric shell can be simplified assuming there is no *shell-crossing* (we discuss this hypothesis below) ensuring the mass conservation

$$\frac{1 + \Delta}{1 + \Delta_i} = \mathcal{R}^{-3}, \quad (74)$$

where  $\Delta_i$  is the initial mass contrast profile of the Lagrangian shell  $\Delta_i = \Delta(\chi(t_i), t_i)$  while  $\Delta$  is the evolved mass contrast  $\Delta = \Delta(\chi, t)$ . We also introduce the logarithmic scale factor  $\tau$  defined through

$$\frac{d\tau}{d \log(a)} := \sqrt{\frac{\Omega_m}{2}}. \quad (75)$$

For  $\Lambda$ CDM, assuming  $\tau(a_i) = 0$  we have

$$\tau(a) = \frac{\sqrt{2}}{3} \left[ \operatorname{arctanh} \left( \Omega_{m,i}^{-1/2} \right) - \operatorname{arctanh} \left( \Omega_m^{-1/2} \right) \right]. \quad (76)$$

With this new parametrization, the equation of motion for each concentric shell (see equation 72) reaches

$$\boxed{\frac{\partial^2 \mathcal{R}}{\partial \tau^2} + \frac{1}{\sqrt{2\Omega_m}} \frac{\partial \mathcal{R}}{\partial \tau} = \mathcal{R} - \frac{1 + \Delta_i}{\mathcal{R}^2}} \quad (77)$$

Equation (77) describes the non-linear gravitational evolution of each shell until shell-crossing. Even if it does not appears now, the formulation equation (77) can be simply extended to any cosmologies including extensions of gravity as we will show it in forthcoming papers (Alimi & de Fromont 2017b; de Fromont & Alimi in preparation). The initial conditions for this differential problem are given by

$$\mathcal{R}(t_i) = 1 \quad (78)$$

together with the first derivative  $\partial_\tau \mathcal{R}(t_i)$ . It can be estimated from the high-redshift solution where the field follows the Zel'dovich dynamic (see Appendix B)

$$\frac{\partial \mathcal{R}}{\partial \tau}(t_i) = -\sqrt{\frac{2}{\Omega_{m,i}}} \frac{\Delta_i}{3} \frac{d \log(D)}{d \log(a)} \Big|_{t_i} := -\sqrt{\frac{2}{\Omega_{m,i}}} \frac{\Delta_i}{3} f(t_i), \quad (79)$$

where  $f(t_i)$  is the linear growth rate evaluated at the initial time  $t_i$ . The non-linearly evolved profile  $\Delta$  is obtained by solving numerically equation (77) and using equation (74) for any initial profile  $\Delta_i$ .

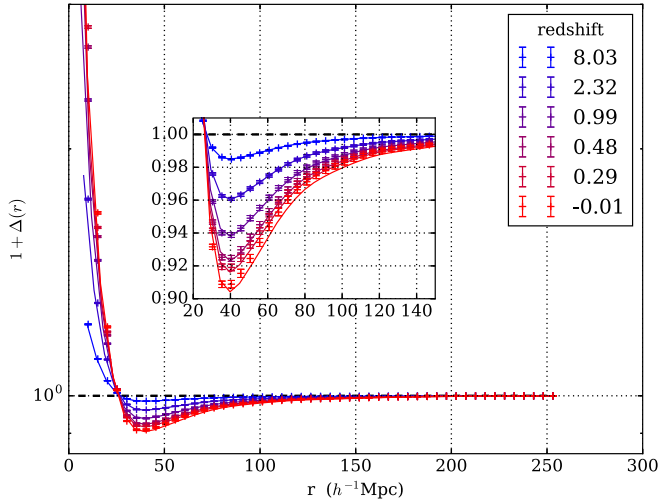


**Figure 12.** Comparison between average numerical profiles and the spherical evolution of the corresponding average primordial numerical matter profile for  $z \simeq 8$  to  $z = 0$  (see text). Points and their associated error bars are the numerical measures for the corresponding redshift while full lines are the spherical evolution of the primordial profile at  $z \simeq 8$ . The computation has been performed using the  $2048^3$  particles simulation with a box size of  $5184 h^{-1} \text{ Mpc}$  in  $\Lambda\text{CDM}$  cosmology and for  $R_1 = 25 h^{-1} \text{ Mpc}$ . All single profiles have been detected from central haloes of mass  $M_h \simeq 2.50 \pm 0.13 \times 10^{14} h^{-1} M_\odot$  at  $z = 0$ .

#### 4.2 Testing the spherical approximation for the evolution of CoSpheres

The validity of the spherical evolution can be tested using the numerical simulations.

At  $z = 0$ , we select haloes with the same  $R_1$ . For each halo detected we apply the ‘backward’ procedure discussed in Section 2.2.3 to build the profile of its progenitor. Stacking these primordial profiles leads to the ‘initial average profile’. This numerical profile is then taken as an input for the spherical dynamics as studied in Section 4.1.

We thus obtain a spherically evolved profile which can be compared to the numerical one at  $z = 0$ .

In Fig. 12, we plot both this *spherically evolved* profile (from  $z \simeq 8$  to  $z = 0$ ) and the numerical profile for  $R_1 = 25 h^{-1} \text{ Mpc}$ . For all redshift, the agreement between the simulation and the spherical evolution is excellent. On small scales however, typically  $r \leq 5 h^{-1} \text{ Mpc}$ , the spherical dynamics fails to almost 5 per cent to 10 per cent. It is not surprising that the central overdense core is not well reproduced by a spherical dynamics but this work focuses on much larger scales where SC provides an excellent dynamical model.

On larger scales, such accuracy is neither reachable with the Eulerian linear nor Zel’dovich dynamics. In Fig. 13, we plot the differences at  $z = 0$  resulting from various dynamical models in the same  $\Lambda\text{CDM}$  cosmology. Here, we used a theoretical mass profile computed from our formalism (see Section 3.2) with realistic shape parameters  $\nu$ ,  $x$  and  $\nu_1$  (close to unity) and we evolved this profile until  $z = 0$  for each model. We choose to show these differences on a void profile, i.e. central underdense minima. The argument is exactly symmetric for central overdensities. The Eulerian linear theory (blue lines) is clearly ruled out on non-linear scales, i.e. for scales typically smaller than  $20 h^{-1} \text{ Mpc}$ . As expected, linear theory, SC and Zel’dovich approximations agree on linear scales. The Zel’dovich approximation reproduces the spherical dynamics with a precision of  $\sim 5$  per cent on the mass contrast profile on large scales but only  $\sim 10$  per cent on the velocity profile. On smaller scales (inside the internal zone,  $r < R_1$ ), the Zel’dovich approximation fails to almost 30 per cent. The inaccuracy of the Zel’dovich dynamics cannot be neglected in a precision cosmology era since it could be misinterpreted as a cosmological imprint (Alimi & de Fromont 2017b; de Fromont & Alimi in preparation).

Spherical dynamics is no longer valid in regions where collapse occurred (the shell reaches the singularity  $r = 0$ ) and if any shell crosses an other one (i.e. when  $\partial\chi/\partial\chi_i = 0$ ). But these two limitations are not really relevant for our purpose due to the size of the considered scales. As a matter of fact, the initial radii of shells that collapse in a finite time are very small, typically of the order of the halo size (fraction or order of  $h^{-1} \text{ Mpc}$ ). In the symmetric case of a

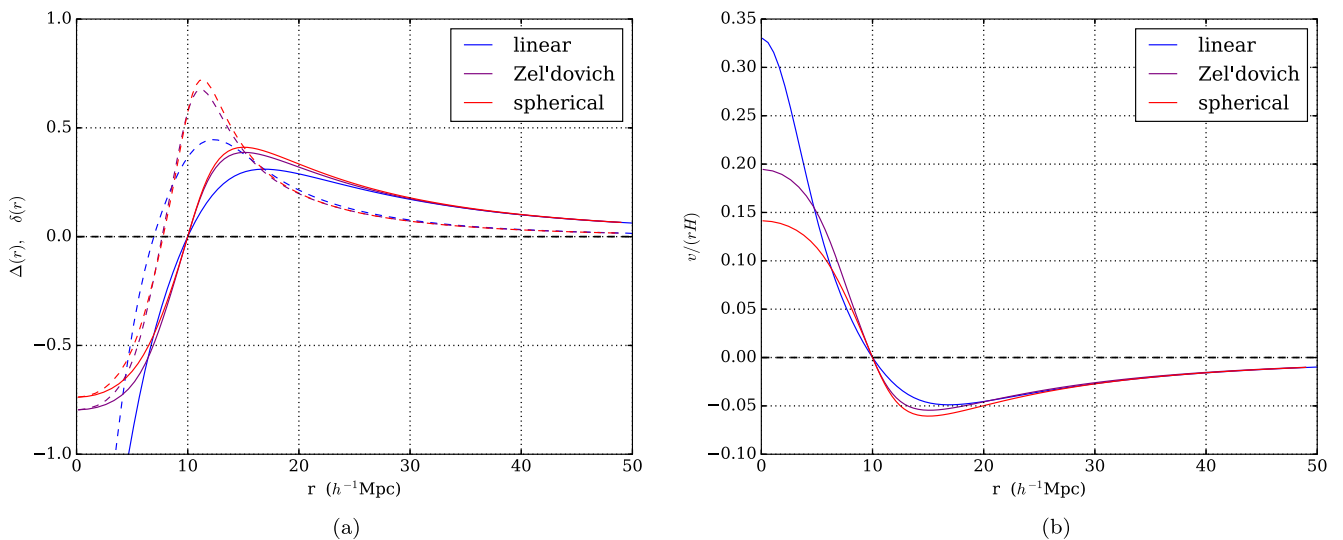


**Figure 13.** Comparison of the various dynamical approximations at  $z = 0$  for a central minimum at  $z = 0$ . Each curve corresponds to the same initial profile evolved with a different dynamical approximation. The Eulerian linear dynamics is in blue, the Zel’dovich approximation is in purple and the full SC is in red. The deviation appears strongly on velocity profiles than on matter profiles. (a) Mass and density contrast at  $z = 0$  for  $R_1 = 10 h^{-1} \text{ Mpc}$ . The full lines correspond to the mass contrast  $\Delta(r)$  while the dashed curves correspond to  $\delta(r)$ . (b) Velocity contrast profile  $\Delta_{\text{vel}}(r) = v/(rH)$  (see equation 86).



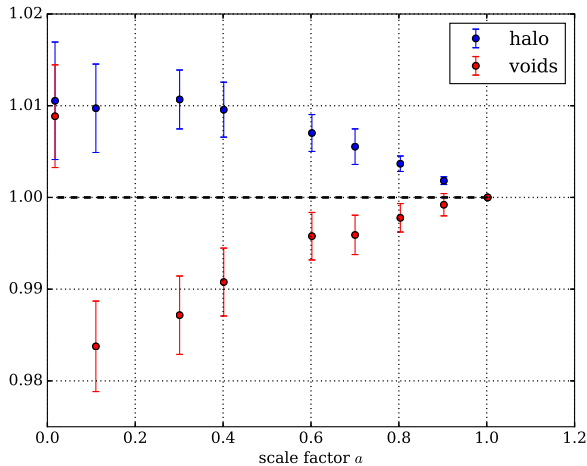


**Figure 14.** Redshift evolution of the ratio  $R_1(z)/R_1(0)$  in comoving coordinates. This figure is obtained using 5000 profiles around haloes with  $M_h \sim 1.5 \times 10^{13} h^{-1} M_\odot$  and the same number of voids without density criteria. For each redshift we compute the distribution for  $R_1(z)/R_1(0)$  from which we estimate its mean (points) and the standard error on the mean (error bars). The ratio  $R_1(z)/R_1(0)$  is thus conserved with a precision better than 2 per cent.

central underdensity, the matter field expands such that there is no possible collapse on to  $r = 0$ . Moreover for compensated cosmic regions with realistic values for the shape parameter  $\nu$ ,  $x$  and  $\nu_1$  (close to unity), radial shell-crossing always occurs deep in our future ( $z \ll 0$ ). Note that the shell-crossing time  $t_{sc}$  of each shell can be easily computed given the initial profile. For example, in the Zel’dovich approximation it satisfies  $D(t_{sc})/D(t_i) = 1 + 1/(\delta_i - 2/3\Delta_i)$ , where both  $\delta_i$  and  $\Delta_i$  are evaluated at the same initial radius  $r_i$ .

### 4.3 Dynamical evolution of the matter field around the compensation radius

#### 4.3.1 Evolution of the compensation radius

As was already mentioned in Fig. 7, the compensation radius is a conserved comoving quantity. This fundamental property is clear from the theoretical point of view. For  $r = R_1$  we have  $\Delta_i(R_1) = 0$  and the only solution of equation (77) compatible with the initial conditions equations (78) and (79) is  $\mathcal{R}(t) = 1$ , leading to  $R_1 \propto a$ .

Physically, since the average density in the closed sphere of radius  $R_1$  equals the background density, this sphere evolves exactly as a closed bubble in the Universe and is consequently comoving.

This property stands in a spherical dynamic but initial inhomogeneities are very unlikely to be spherically symmetric (Bardeen et al. 1986). Using numerical simulations, we can follow the redshift evolution of  $R_1$  for every CoSphere. In Fig. 14, we plot the mean and the dispersion of the distribution  $R_1(z)/R_1(0)$  as a function of redshift for both haloes and void. For the whole range of redshift, comoving  $R_1$  is constant with a precision better than 2 per cent for voids and 1 per cent for haloes. There is however a clear tendency of increasing  $R_1$  for voids and decreasing  $R_1$  for haloes. These small evolutions result probably from primordial anisotropies. They remain sufficiently small so that the spherical approximation holds. A deeper understanding of this small evolution goes beyond the scope of this paper.

#### 4.3.2 The evolution of the compensation density $\delta_1$

The compensation density contrast  $\delta_1$  defined as  $\delta_1 := \nu_1 \sigma_0$  is an Eulerian quantity, being defined at a fixed comoving position  $\chi_1 = R_1/a$ . To derive its Eulerian dynamics, we consider two points initially located at an infinitesimal distance from the compensation radius  $\chi_i^\pm := \chi_1 \pm \epsilon$  where  $\epsilon \ll 1$ . Since we consider two points in the infinitesimal range  $\pm\epsilon$  we have (see equation B2)

$$\mathcal{R}^\pm(t) = 1 - (\pm\epsilon) \frac{\delta_1}{\chi_1} \left( \frac{D(t)}{D(t_i)} - 1 \right) + \mathcal{O}(\epsilon^2), \quad (80)$$

where  $\delta_1$  is assumed to be the value of the local density contrast in the initial conditions. The same quantity at any time  $t \neq t_i$  is explicitly noted with its time dependence  $\delta_1(t)$ . At first order in  $\epsilon$ , the position of each shell  $\chi^\pm(t)$  at any time  $t$  reduces to

$$\chi^\pm(t) = \chi_1 \pm \epsilon \left[ 1 - \delta_1 \left( \frac{D(t)}{D(t_i)} - 1 \right) \right] + \mathcal{O}(\epsilon^2). \quad (81)$$

Using the mass conservation equation (74), the mass contrast for each shell is

$$\Delta^\pm(t) = \pm\epsilon \frac{3\delta_1}{\chi_1} \frac{D(t)}{D(t_i)} + \mathcal{O}(\epsilon^2). \quad (82)$$

Using  $\delta_1(t) = R_1/3\Delta'(R_1)$  together with  $\Delta'(R_1) = \lim_{\epsilon \rightarrow 0} (\Delta^+ - \Delta^-)/(\chi^+ - \chi^-)$ , we get

$$\delta_1(t) = \delta_1 \frac{\tilde{D}(t)}{1 - \delta_1 (\tilde{D}(t) - 1)}, \quad (83)$$

with the normalized linear growth factor  $\tilde{D}(t) = D(t)/D(t_i)$ . This solution corresponds to a one-dimensional Zel’dovich dynamics (Zel’dovich 1970). However, this solution is exact within the SC. Note that for an initial negative compensation density ( $\delta_1 < 0$  which corresponds to a central overdensity, i.e. a maximum), the asymptotic value is  $-1$  and  $\delta_1(t)$  does not diverges to  $-\infty$  as expected in the linear regime. The linear regime is recovered for  $\delta_1[1 - \tilde{D}(t)] \ll 1$  where equation (83) reduces to the usual linear relation

$$\delta_1(t) \simeq \delta_1 \tilde{D}(t). \quad (84)$$

We stress that equation (83) applies only for the very particular radius  $r = R_1$  and cannot be extended to every point of the density profile where it would be, at best, a dynamical approximation. Equation (83) contains its own information about shell-crossing. Indeed, for the particular time  $t_{sc}$  satisfying

$$\frac{D(t_{sc})}{D(t_i)} = \frac{1 + \delta_1}{\delta_1}. \quad (85)$$

The denominator of equation (83) vanishes, leading to  $\delta_1(t_{sc}) \rightarrow \infty$ . This divergence is only possible for positive values of  $\delta_1$ , i.e. for central underdensity.<sup>8</sup> The divergence of the local density illustrates the apparition of caustics in the density field, due to the possible crossing of different shells at this particular radius where matter accumulates.

High values of  $\nu_1$  can lead to a collapse of the surrounding overdense belt on to the central minimum. This is known as the *void-in-cloud* problem (Sheth & van de Weygaert 2004). For such voids, the compensation belt is deeply affected by shell-crossing and the compensation radius is no longer conserved (it decreases with time). The smallest  $\nu_1$  leading to radial shell-crossing today depends on  $R_g$ , the Gaussian smoothing scale of the power spectrum.

<sup>8</sup> Remember that the sign of  $\delta_1$  is the opposite of the sign of the central extremum.

In  $\Lambda$ CDM cosmology, this critic  $\nu_1$  (computed from equation 85) evolves from  $\nu_1 \simeq 0.2$  for  $R_g \rightarrow 0$  and crosses  $\nu_1 = 1$  for  $R_g \simeq 4 h^{-1}$  Mpc. This illustrates that the shell-crossing mechanism behaves differently according to the smoothing scale. In our case, the power spectrum is smoothed on the scale equivalent to the size of the coarse grid cell of the simulation to cut the power on smaller scales (in the reference simulation we have  $R_{\text{cell}} = 1.26 h^{-1}$  Mpc). For this smoothing size, the shell-crossing threshold is  $\nu_1 \simeq 0.65$ . As will be shown in Alimi & de Fromont (2017a), this value is much larger than the typical values of  $\nu_1$ , which are expected to be less than  $\nu_1 \sim 0.03$ . This ensures that spherical shell-crossing is very rarely reached in voids and the void-in-cloud effect can thus be neglected, excepted for some very rare events.

Note that this is not in contradiction with the most common definition criterion for voids, namely that they are enclosed by shell-crossed boundaries (Bertschinger 1985; Sheth & van de Weygaert 2004). Indeed, as was already pointed out in Sheth & van de Weygaert (2004), this shell-crossing does not appear in sufficiently smoothed profiles, which is the case for realistic CoSphere profiles. The clumpy structuration on small scales where shell-crossing locally happened to form virialized structures is not relevant for spherical averaged profiles due to the large volume of radial shells. For central maximum, the shell at  $r = R_1$  acts as a gravitational repeller, avoiding caustic formation.

#### 4.3.3 The local velocity field

Since the Lagrangian displacement  $\mathcal{R}$  obeys a second-order differential equation (see equation 77), the field is fully characterized by  $\mathcal{R}$  and its first derivative. In other word, the radial peculiar velocity (linked to the time derivative of  $\mathcal{R}$ ) carries a complementary information. We thus defined the velocity contrast  $\Delta_{\text{vel}}$  as

$$\dot{r} = rH(t)[1 + \Delta_{\text{vel}}(r, t)] \quad (86)$$

measuring the radial peculiar velocity in units of the Hubble flow  $rH$ . This dimensionless quantity is computed in the Lagrangian formalism as

$$\Delta_{\text{vel}}(r, t) := \frac{\partial \log \mathcal{R}}{\partial \log a} = \sqrt{\frac{\Omega_m}{2}} \frac{\partial \log(\mathcal{R})}{\partial \tau} \quad (87)$$

and satisfies  $\Delta_{\text{vel}}(R_1) = 0$  during the whole evolution. In the Zel'dovich regime, mass and velocity contrast profiles are directly proportional

$$\Delta_{\text{vel}}(r, t) = -\frac{\Delta(r, t)}{3} \times f(t), \quad (88)$$

where  $f(t)$  is the linear growth rate. We also define the velocity divergence  $\delta_{\text{vel}}(r) = \nabla \cdot \mathbf{v}/(3H)$  linked to the velocity contrast by

$$\Delta'_{\text{vel}}(r) = \frac{3}{r} [\delta_{\text{vel}}(r) - \Delta_{\text{vel}}(r)]. \quad (89)$$

Using a similar computation than in Section 4.3.2, we can compute the exact non-linear evolution of  $\delta_{\text{vel}}$  around  $R_1$

$$\delta_{\text{vel}}(R_1, t) = -\frac{f(t)}{3} \frac{\delta_1 \tilde{D}(t)}{1 - \delta_1 (\tilde{D}(t) - 1)}. \quad (90)$$

With the explicit expression for  $\delta_1(t)$  (see equation 83), we get

$$\frac{\delta_{\text{vel}}(R_1, t)}{\delta_1(t)} = -\frac{f(t)}{3}, \quad (91)$$

which is the standard relation linking the velocity divergence and the density field in the linear regime. However, in the SC model,

it is an exact result at any redshift for  $r = R_1$ . For other radii, the previous relation equation (91) is only valid in linear regime.

Equation (91) provides an efficient way to evaluate exactly the linear growth rate using CoSpheres. We emphasize that equation (91) allows to measure the linear growth rate on non-linear scales, it only necessitate to consider structures with small compensation radii. The measure of the linear growth rate, for example from redshift-space distortions, is beyond the scope of this paper and will be investigated in a forthcoming paper (Alimi & de Fromont 2017b).

#### 4.4 Reconstructing profiles at $z = 0$

In Section 3, we have shown that the large-scale matter profile of CoSpheres can be precisely reconstructed using GRF (see equation 51). Theoretical profiles are parametrized by three independent shape parameters  $\nu$ ,  $x$ ,  $\nu_1$  (see Section 3.2) in addition to the compensation radius.

In Section 4.2, we have shown that the SC model provides a good description of the gravitational evolution of these large-scale profiles. Combining the initial conditions and the dynamics, we show in this section that CoSpheres can be precisely reconstructed until  $z = 0$  with a high accuracy on a large radial domain.

At  $z = 0$ , we build the average mass contrast profiles of CoSphere in numerical simulations (see Section 2.2.2). For each  $R_1$  it provides an average profile together with its dispersion (computed as the standard error on the mean). For each profile at  $z = 0$ , the reconstruction procedure consists in finding the appropriate shape parameters  $\nu$ ,  $x$  and  $\nu_1$  in GRF (see equation 51). Practically, we iterate over the shape parameters and minimize a standard  $\chi^2$  at  $z = 0$  using the spherical evolution of the GRF expected profile.

In Fig. 15, we show the reconstructed mass contrast profiles at  $z = 0$  for  $R_1 = 20$  and  $R_1 = 40 h^{-1}$  Mpc. The reconstructed CoSphere reproduces the numerical profile with a very high accuracy (a deviation smaller than 1 per cent) on a large spatial domain. Again we emphasize that the peak parameters  $\nu$  and  $x$  provide the description of the field around the central extremum whereas  $\nu_1$  defined at  $r = R_1$  drives the shape on larger scales (see Fig. 9). Fig. 15 shows that the reconstruction procedure works for various neighbourhoods. Although we considered the same haloes (same mass), we probe various neighbourhoods by varying the compensation scale  $R_1$ . A large compensation radius describes a local extremum located in a huge over-/undermassive region. On the other hand, the same peak with a smaller  $R_1$  corresponds to a local extrema in an small overdense ‘island’ isolated in a larger underdense region.

In Fig. 16, we show the reconstruction of CoSphere profiles defined around haloes with different masses, namely  $M_h \sim 3.6 \times 10^{12} h^{-1} M_\odot$  (extracted from the simulation with  $1024^3$  particles and a box size  $648 h^{-1}$  Mpc) and  $M_h \sim 2.5 \times 10^{14} h^{-1} M_\odot$  (extracted from the simulation with  $2048^3$  particles and a box size  $5184 h^{-1}$  Mpc) for the same compensation radius  $R_1 = 20 h^{-1}$  Mpc. Varying the mass of the central halo changes the amplitude of matter fluctuation, and thus the profile itself. Increasing the mass of the central halo raises the primordial peak threshold, i.e. selects peaks with higher  $\nu$ . Since the central extrema is correlated to its surrounding environment, large  $\nu$  induce higher  $\delta_1$  and thus  $\nu_1$ . In other words, a massive halo is more likely to sit in a deepest void than a lighter halo.

Finally, the exact same reconstruction can be done for central underdense regions identified to cosmic voids. The measured profiles of underdense CoSphere together with their theoretical reconstruction are shown in Fig. 17. We show the reconstruction for two different compensation radii. Here again, CoSphere profiles are well reconstructed on all scales with a very high accuracy, even in the

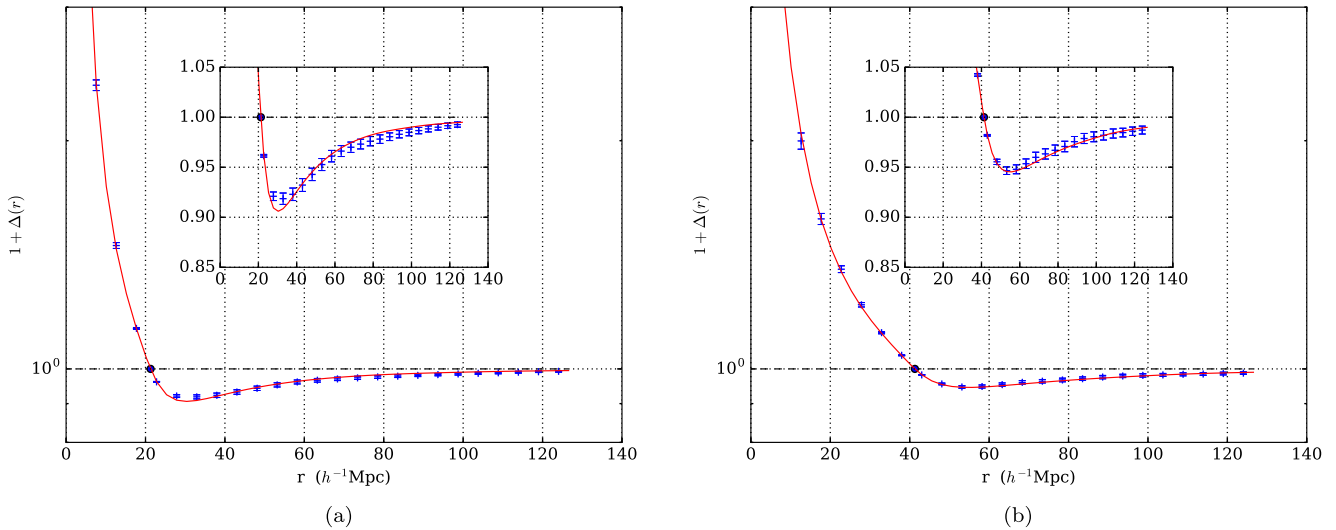


**Figure 15.** Reconstruction of the mass contrast profile  $1 + \Delta(r)$  measured in the simulation at  $z = 0$  (blue points) for haloes of mass  $M_h \sim 3.0 \times 10^{13} h^{-1} M_\odot$ . The red line is the CoSphere curve obtained by minimizing a standard  $\chi^2$  at  $z = 0$  (see text). (a) Mass contrast profile for  $R_1 = 20 h^{-1}$  Mpc and (b) same as panel (a) for  $R_1 = 40 h^{-1}$  Mpc.

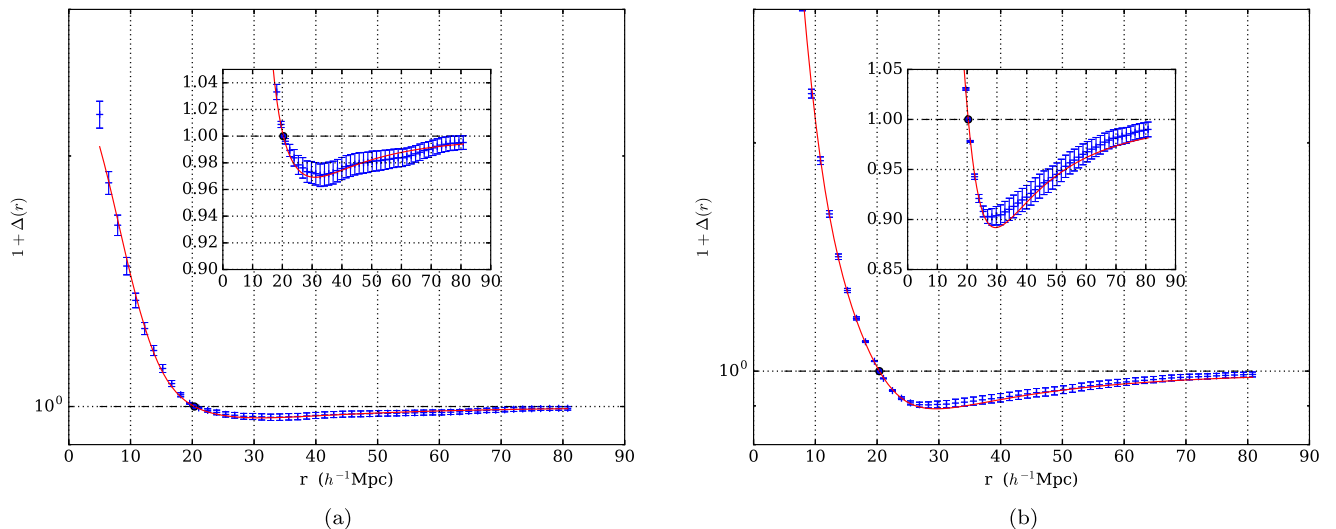


**Figure 16.** Reconstruction of CoSphere profile at  $z = 0$  (blue points) from two different haloes with the same compensation radius  $R_1 = 20 h^{-1}$  Mpc. The red line is the theoretical curve obtained by computing the best shape parameters  $\nu$ ,  $x$  and  $\nu_1$  and spherically evolved until  $z = 0$  (see text). This figures illustrate the mass dependence of the profiles. Matter profiles around heavier haloes are more amplified than the same profiles build from lighter ones. Increasing the mass of the central haloes raises the primordial height  $\nu = \delta(x_0)/\sigma_0$ . Shape parameters are correlated to each other such that it is more likely to get higher  $\nu_1$  when  $\nu$  grows (Alimi & de Fromont 2017a). Heavier haloes will thus induce more amplified profiles on all scales, as it is illustrated in this figure. (a) Mass contrast profile for haloes of mass  $M_h \sim 3.6 \times 10^{12} h^{-1} M_\odot$ . We used here the simulation with  $1024^3$  particles and a box size  $L = 648 h^{-1}$  Mpc. (b) Same as panel (a) for  $M_h \sim 2.5 \times 10^{14} h^{-1} M_\odot$  with the same  $R_1$  in the simulation with  $2048^3$  particles and a box size  $L = 5184 h^{-1}$  Mpc.

central underdense core ( $r \ll R_1/5$ ). This is not surprising since cosmic voids tends to sphericity during the tri-axial expansion, unlike their overdense symmetric (Icke 1984; van de Weygaert 2014). CoSpheres provide thus an efficient physically motivated model that can be used to reproduce large-scale spherical inhomogeneities at any redshift.

## 5 DISCUSSION AND OUTLOOKS

The absence of a physically motivated model for understanding the large-scale matter profiles of compensated cosmic regions is a major difficulty in the precision cosmology era. Extracting reliable cosmological information from such regions, and particularly from voids,

requires a deep understanding of their origin and their evolution. In this paper, we address this issue by generalizing void profiles and introducing CoSpheres. These regions are build explicitly from their compensation property. The particular radius  $R_1$  where the matter field compensate exactly appears to be a fundamental scale for both their origin and their dynamics. This comoving radius isolates closed bubble Universe with a conserved volume during the whole cosmic evolution (see Section 4.3.1).

When defined around central underdense minimum, these regions can be identified to cosmic void, providing a useful theoretical framework for studying both their shape and their evolution. Interestingly, these regions can be also defined around local maximum such as DM haloes. By definition, these regions must be

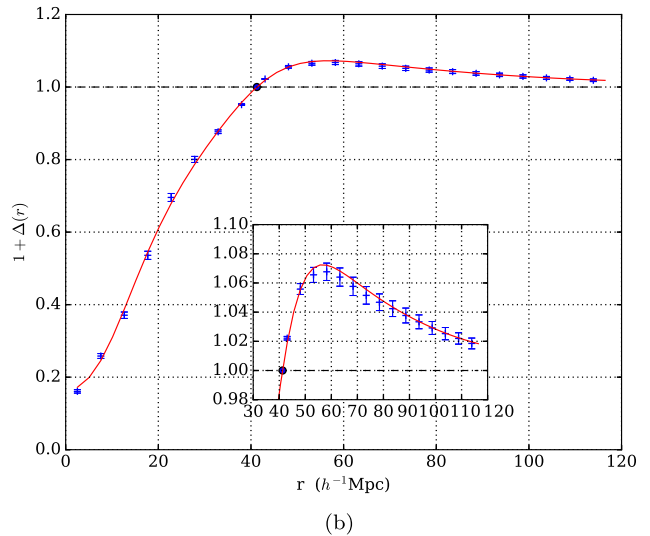
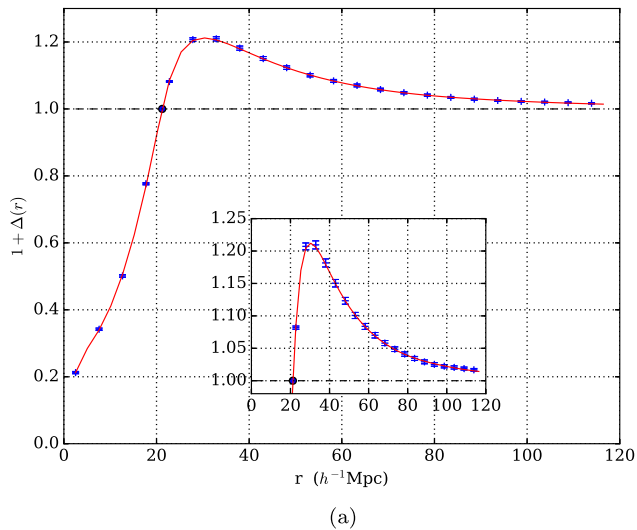


**Figure 17.** Reconstructed CoSphere profile at  $z = 0$  around local underdense minimum. These minima are obtained by smoothing the density field with a Gaussian kernel with  $R_g = 2 h^{-1}$  Mpc. The red line is the theoretical curve obtained from GRF with the best-fitting shape parameters and evolved with a spherical dynamics (see text). It is noticeable that the reconstruction provides an excellent fit on all scales and whatever  $R_1$  although theoretical profiles are determined by three parameters including two parameters defined around  $r = 0$ . (a) Mass contrast profile for  $R_1 = 20 h^{-1}$  Mpc and (b) same as panel (a) for  $R_1 = 40 h^{-1}$  Mpc.

compensated on a finite scale, hence the existence of large underdense regions surrounding over densities.

Using numerical simulations introduced in Section 2.1, we build the averaged profiles of CoSpheres by stacking together regions with the same compensation radius  $R_1$ . These numerical simulations can be used to follow backward in time the evolution of such cosmic structures (see Section 3.3). From these primordial numerical profiles we have shown that CoSpheres are generated from the stochastic fluctuations of the primordial field (see Section 2.2.3 and Fig. 7).

At high redshift the matter field follows a Gaussian statistics. In order to derive the matter profile of CoSpheres in GRF formalism, we have extended the results of Bardeen et al. (1986) by implementing explicitly the compensation conditions equations (5) and (10) (see Section 3). With this original compensation constraint, the spherical density (and mass) contrast profile is now parameterized by four independent – but correlated – shape parameters;  $\nu$  and  $x$  qualifying the central extrema (already introduced by BBKS) while  $\nu_1$  and  $R_1$  characterize the surrounding cosmic environment on larger scales. While the standard BBKS profile was determined on all scales by providing the peak parameters  $\nu$  and  $x$ , our extension allows to probe the same central extremum in various cosmic environments. These physical configurations can be described by the additional shape parameters  $\nu_1$  and  $R_1$  (see Fig. 10). We emphasize that  $\nu$  and  $x$  affect the matter profile on small scales while  $\nu_1$  controls the shape and the amplitude on larger scale, typically around and beyond the compensation radius.

In Section 4.2, we show that the SC model is well suited for the dynamical evolution of CoSpheres whereas neither Zel’dovich nor linear dynamics provide satisfying accuracy. We show that the full non-linear gravitational collapse can be solved analytically around  $R_1$  where it reduces to a one-dimensional Zel’dovich dynamics. We stress that on this particular radius, the Zel’dovich dynamics provides an exact solution for the SC and not only a dynamical approximation. In particular, this implies that the linear growth rate can be exactly estimated on this scale (see equation 91). This emphasizes the relevance of this particular radius. The possibilities to

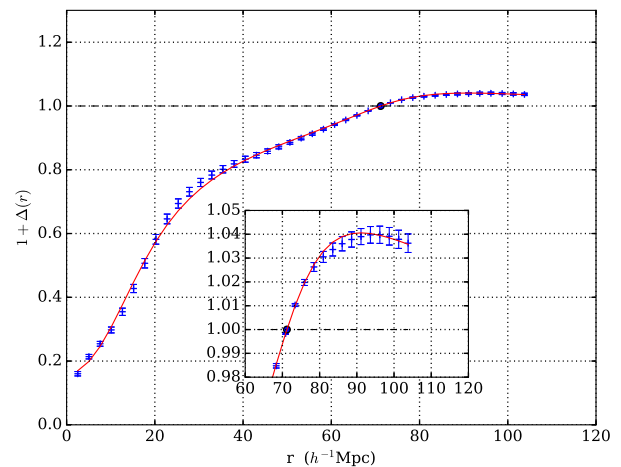


**Figure 18.** Reconstruction of a void profile at  $z = 0$  with a large compensation radius  $R_1 = 70 h^{-1}$  Mpc. The red curve is the CoSphere reconstruction obtained through the procedure discussed in Section 4.4. This figure illustrates the particular elbow around  $r \sim 25 h^{-1}$  Mpc as in Fig. 3. This original feature will be discussed in a following paper Alimi & de Fromont (2017a) and appears as an imprint of the decoupling between the central extrema and its surrounding environment.

use this property and to constrain the underlying cosmology will be discussed in detail in Alimi & de Fromont (2017b) and de Fromont & Alimi (in preparation).

For central minimum, CoSphere can be identified to cosmic voids. Their radial profiles exhibit a characteristic elbow around  $r \sim 20 h^{-1}$  Mpc (see Figs 4b and 18). This elbow is present on both density and mass contrast profile, though it is more pronounced on density profiles (red curve in Fig. 3b). This particular shape property is a characteristic of the definition of our cosmic voids and does not appear clearly in void profiles build from other algorithm (e.g. Hamaus et al. 2014b).

This elbow is a specific feature of our stacking operation which combine profiles with the same compensation radius  $R_1$ . For other



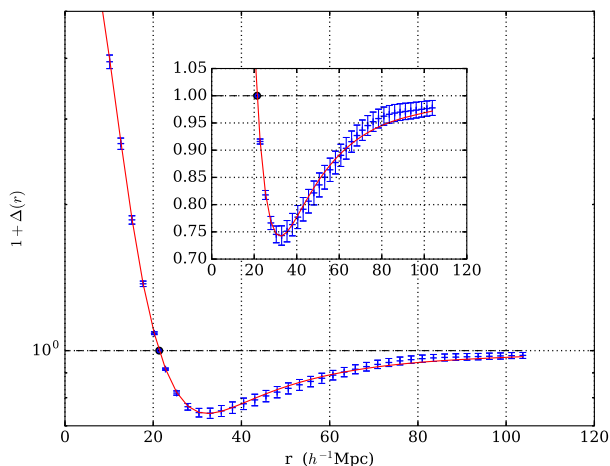


**Figure 19.** Mass contrast profile from central haloes of mass  $M_h \sim 3.0 \times 10^{13} h^{-1} M_\odot$  computed from the *halo field* at  $z = 0$ . This profile is obtained by considering a biased field traced by DM haloes weighted by their mass. The mean density  $\bar{\rho}$  is estimated from the ratio between the total mass of haloes and the volume of the simulations. The red curve is the theoretical reconstruction using CoSphere formalism as discussed in Section 4.4.

void reconstructions based on their effective radius  $R_{\text{eff}}$ , this elbow may be smoothed by the stacking together profiles with various  $R_1$ . As will be discussed in Alimi & de Fromont (2017a), this elbow is the imprint of the progressive decorrelation between the central extrema and the surrounding cosmic environment.

We stress that our work allows a common description for the formation of both cosmic void and large-scale profile surrounding haloes. The efficiency of the reconstruction procedure (see Section 4.4) emphasizes  $R_1$  as a fundamental scale carrying the memory of the primordial Universe and qualifying cosmic structures.

Finally, all the results presented in this paper assume a non-biased or distorted CDM field. In realistic surveys however, we do not have access to the full CDM field but rather to its discrete tracers as galaxies or galaxy cluster. In a  $N$ -body simulation, these tracers can be modelled from DM haloes since galaxies are more likely to form in potential wells generated by DM collapse. As a proof of concept we show in Fig. 19 the reconstructed matter profile obtained from the field traced only by DM haloes. The global shape of profiles is not changed when using the biased field and CoSpheres can still be clearly identified. The agreement between numerical profiles (blue points) and reconstructed theoretical profile (in red) is again excellent on all scales. The only modification with the previous matter profiles reduces, in a first approximation, to the introduction of a linear bias  $b$  such as  $\delta_{\text{haloes}} = b \times \delta_{\text{CDM}}$  without affecting the shape of CoSpheres. For cosmic voids, the linearity of the bias has been studied in Pollina et al. (2017) where it was shown to be a very good approximation, whatever the tracer population (galaxies, galaxy clusters and AGN).

## ACKNOWLEDGEMENTS

We thank the anonymous referee for useful comments. We also thank Jean Padeloup for his help in developing numerical tools for void detection in numerical simulations. This work was granted access to HPC resources of TGCC and IDRIS through allocations made by Grand Equipement National de Calcul Intensif (GENCI) in the framework of the ‘Grand Challenge’ DEUS.

## REFERENCES

- Achitouv I., 2017, *Phys. Rev. D*, 96, 083506
- Achitouv I., Baldi M., Puchwein E., Weller J., 2016, *Phys. Rev. D*, 93, 103522
- Achitouv I., Blake C., Carter P., Koda J., Beutler F., 2017, *Phys. Rev. D*, 95, 083502
- Alimi J.-M., de Fromont P., 2017a, preprint (arXiv:1709.09916)
- Alimi J.-M., de Fromont P., 2017b, submitted
- Alimi J.-M., Füzfa A., Boucher V., Rasera Y., Courtin J., Corasaniti P.-S., 2010, *MNRAS*, 401, 775
- Alimi J.-M. et al., 2012, DEUS Full Observable LCDM Universe Simulation: the numerical challenge. IEEE Computer Society Press, CA, USA, SC2012, Article No. 73,
- Bardeen J. M., Bond J. R., Kaiser N., Szalay A. S., 1986, *ApJ*, 304, 15
- Bertschinger E., 1985, *ApJS*, 58, 39
- Bertschinger E., 1987, *ApJ*, 323, L103
- Cai Y.-C., Padilla N., Li B., 2015, *MNRAS*, 451, 1036
- Caldwell R. R., Kamionkowski M., 2009, *Annu. Rev. Nucl. Part. Sci.*, 59, 397
- Colberg J. M., Sheth R. K., Diaferio A., Gao L., Yoshida N., 2005, *MNRAS*, 360, 216
- Courtin J., Rasera Y., Alimi J.-M., Corasaniti P.-S., Boucher V., Füzfa A., 2011, *MNRAS*, 410, 1911
- Guillet T., Teyssier R., 2011, *J. Comput. Phys.*, 230, 4756
- Gunn J. E., Gott J. R., 1972, *ApJ*, 176, 1
- Hamaus N., Wandelt B. D., Sutter P., Lavaux G., Warren M. S., 2014a, *Phys. Rev. Lett.*, 112, 041304
- Hamaus N., Sutter P. M., Wandelt B. D., 2014b, *Phys. Rev. Lett.*, 112, 251302
- Hamaus N., Sutter P., Lavaux G., Wandelt B. D., 2015, *J. Cosmol. Astropart. Phys.*, 2015, 036
- Hamaus N., Pisani A., Sutter P., Lavaux G., Escoffier S., Wandelt B. D., Weller J., 2016, *Phys. Rev. Lett.*, 117
- Hehl F. W., Mccrea J. D., 1986, *Found. Phys.*, 16, 267
- Icke V., 1984, *MNRAS*, 206, 1p
- Komatsu E. et al., 2009, *ApJS*, 180, 330
- Kowalski M. et al., 2008, *ApJ*, 686, 749
- Lahav O., Lilje P. B., Primack J. R., Rees M. J., 1991, *MNRAS*, 251, 128
- Lavaux G., Wandelt B. D., 2010, *MNRAS*, 403, 1392
- Lavaux G., Wandelt B. D., 2012, *ApJ*, 754, 109
- Lewis A., Challinor A., Lasenby A., 2000, *ApJ*, 538, 473
- Mao Q., Berlind A. A., Scherrer R. J., Neyrinck M. C., Scoccimarro R., Tinker J. L., McBride C. K., Schneider D. P., 2017, *ApJ*, 835, 160
- Neyrinck M. C., 2008, *MNRAS*, 386, 2101
- Padmanabhan T., 1993, *Structure Formation in the Universe*. Cambridge Univ. Press, Cambridge
- Pan D. C., Vogeley M. S., Hoyle F., Choi Y., Park C., 2012, *MNRAS*, 421, 926
- Park D., Lee J., 2007, *Phys. Rev. Lett.*, 98
- Peacock J. A., 1998, *Cosmological Physics* (Cambridge Astrophysics). Cambridge Univ. Press, Cambridge
- Peebles P. J. E., 1980, *Large-Scale Structure of the Universe*. Princeton Univ. Press, Princeton, NJ
- Perlmutter S. et al., 1999, *ApJ*, 517, 565
- Platen E., Weygaert R. V. D., Jones B. J. T., 2007, *MNRAS*, 380, 551
- Pollina G., Hamaus N., Dolag K., Weller J., Baldi M., Moscardini L., 2017, *MNRAS*, 469, 787
- Prunet S., Pichon C., Aubert D., Pogosyan D., Teyssier R., Gottloeber S., 2008, *ApJS*, 178, 179
- Rasera Y., Alimi J.-M., Courtin J., Roy F., Corasaniti P.-S., Füzfa A., Boucher V., 2010, in Alimi J.-M., Füzfa A., eds, *AIP Conf. Ser. Vol. 1241, Invisible Universe*. Am. Inst. Phys., New York, p. 1134
- Reverdy V. et al., 2015, *Int. J. High Perform. Comput. Appl.*, 29, 249
- Ricotti M., Pontzen A., Viel M., 2007, *ApJ*, 663, L53
- Riess A. G. et al., 1998, *AJ*, 116, 1009
- Sheth R. K., van de Weygaert R., 2004, *MNRAS*, 350, 517



- Silvestri A., Trodden M., 2009, Rep. Prog. Phys., 72, 096901  
 Sutter P. M., Pisani A., Wandelt B. D., Weinberg D. H., 2014, MNRAS, 443, 2983  
 Teyssier R., 2002, A&A, 385, 337  
 van de Weygaert R., 2014, Proc. IAU, 11, 493  
 van de Weygaert R., Bertschinger E., 1996, MNRAS, 281, 84  
 van de Weygaert R., Platen E., 2011, Int. J. Mod. Phys.: Conf. Ser., 01, 41  
 Wang L., Steinhardt P. J., 1998, ApJ, 508, 483  
 Zel'dovich Y. B., 1970, A&A, 5, 84

## APPENDIX A: SHIFTING THE CENTRE OF MASS

The primordial profiles computed in equations (51) and (36) have been derived within the GRF formalism assuming that the position  $\mathbf{x}_0$  of the central extrema is perfectly known. However, the reconstruction procedure of the averaged profiles at higher redshift as introduced in Section 3.3 may induce a shift between the exact position of the local extrema  $\mathbf{x}_0$  and its estimation  $\mathbf{x}_c$ . In this section, we evaluate the consequence of missing this exact position.

We assume that the density profile centred on the real extrema  $\langle \delta \rangle(r_i)$  is given by equation (36) where  $r_i$  denotes the comoving distance from the real extrema  $\mathbf{x}_0$ , i.e.  $r_i = |\mathbf{x}_0 - \mathbf{x}|$ . We want to evaluate the density contrast on the shell located at a radius  $r$  where  $r$  is measured from the estimated (but *wrong*) centre  $\mathbf{x}_c$  shifted by  $\mathbf{x}_c := \mathbf{x}_0 + \mathbf{R}$ . In other words we note  $r = |\mathbf{r}| = |\mathbf{x}_c - \mathbf{x}|$ .

Let us define  $\varphi$  such as  $\mathbf{R} \cdot \mathbf{r} = R \cdot r \cdot \cos(\varphi)$ . Following equation (36), the spherical density contrast can be written as an Hankel Transform

$$\langle \delta \rangle(r_i) = \int P(k) \times \tilde{\delta}(v, x, v_1, R_1, k) \frac{\sin(kr_i)}{kr_i} dk, \quad (\text{A1})$$

where  $\tilde{\delta}$  is a linear function of  $v, x$  and  $v_1$  and depends non-linearly in  $k$  and  $R_1$  (see equation 36) while  $P(k)$  is the linear power spectrum. The ‘reconstructed’ density contrast  $\langle \delta \rangle'(r)$  around the position  $\mathbf{x}_c$  at a radius  $r$  is thus given by averaging  $\langle \delta \rangle$  on the shifted sphere of radius  $r$  around  $\mathbf{x}_c$

$$\langle \delta \rangle'(r) = \frac{1}{2} \int_0^\pi \sin(\varphi) \langle \delta \rangle \left( \sqrt{r^2 + R^2 - 2rR \cos(\varphi)} \right) d\varphi. \quad (\text{A2})$$

Using the explicit expression equation (A1) for  $\langle \delta \rangle$  we find

$$\langle \delta \rangle'(r) = \int P(k) \times \tilde{\delta}(v, x, v_1, R_1, k) \frac{\sin(kr)}{kr} \times \frac{\sin(kR)}{kR} dk. \quad (\text{A3})$$

Thus, the shifted profile  $\langle \delta \rangle'(r)$  takes exact same form than the un-shifted profile  $\langle \delta \rangle(r)$  given by equation (36) with an effective power-spectrum  $P_{\text{eff}}(k)$  given by

$$P(k) \xrightarrow{\mathbf{x}_0 + \mathbf{R}} P_{\text{eff}}(k) := P(k) \times \frac{\sin(kR)}{kR}. \quad (\text{A4})$$

Of course, for  $R \rightarrow 0$  we recover the usual profile but for  $R \neq 0$ , the profile implies an effective power spectrum smoothed on the shifting scale  $R$ . Note also that missing the right centre of mass leads to non-isotropic profiles but here we focus only the spherically average profile. The mass contrast profile  $\langle \Delta \rangle$  (see equation 51) is affected by the exact same factor, i.e. it is written exactly as equation (51) but with the effective spectrum given by equation (A4).

## APPENDIX B: HIGH-REDSHIFT SOLUTION AND THE ZEL'DOVICH APPROXIMATION

The dynamical equation (77) can be solved exactly orders by orders for  $\mathcal{R}$  (and for each radius  $r_i$ ) with the series

$$\mathcal{R}(t) = 1 + \sum_{n \geq 1} \eta_n(t) \Delta_i^n, \quad (\text{B1})$$

where each function  $\eta_n(t)$  depends only on  $t$  and  $\eta_n(t_i) = 0$ . The solution equation (B1) is the exact solution for the Lagrangian perturbation theory in spherical coordinates which is valid until shell-crossing.

### B1 High-redshift solution

In the very high-redshift regime ( $z \gg 1$ ), the initial mass contrast  $\Delta_i$  satisfies  $\Delta_i \ll 1$  for all initial radius  $r_i$  (since  $\Delta_i \sim \sigma_0$ ). The 0th order term of equation (B1) corresponds to the linear Eulerian theory  $\delta(\mathbf{x}, t) \propto D(t)\delta(\mathbf{x}, t_i)$ .

Let us now consider the first-order term

$$\mathcal{R}(t) \simeq 1 + \eta_1(t) \Delta_i + \mathcal{O}(\Delta_i^2), \quad (\text{B2})$$

with  $\eta_1(t_i) = 0$ . In this regime, the right-hand term of equation (77) reduce to

$$\mathcal{R} - \frac{1 + \Delta_i}{\mathcal{R}^2} \xrightarrow{\Delta_i \ll 1} \Delta_i (3\eta_1(t) - 1). \quad (\text{B3})$$

If we define  $J$  such as  $\eta_1 = (J - 1)/3$ , using equation (B3), it is easy to show that  $J(t)$  satisfies

$$\frac{d^2 J}{dt^2} + 2H(t) \frac{dJ}{dt} = \frac{3}{2} H^2(t) \Omega_m(t) J(t), \quad (\text{B4})$$

with  $J(t_i) = 1$ . Equation (B4) is exactly the equation solved by the linear growth factor  $D(t)$ , thus, using  $J(t_i) = 1$  we deduce that in this weak field regime,  $\eta(t)$  is given by

$$\eta_1(t) = -\frac{1}{3} \left( \frac{D(t)}{D(t_i)} - 1 \right). \quad (\text{B5})$$

In this regime, the displacement field  $\mathcal{R}$  is given by

$$\mathcal{R}(t) = 1 - \frac{\Delta_i}{3} \left( \frac{D(t)}{D(t_i)} - 1 \right), \quad (\text{B6})$$

where the  $\Delta_i$  and thus  $\mathcal{R}$  depend on the initial position  $r_i$ .

### B2 Link with the Zel'dovich approximation

The Zel'dovich approximation (denoted as ZA; Zel'dovich 1970) consists into approximating the field displacement by its initial value. With our notation, it reaches

$$\chi(\mathbf{q}, t) = \mathbf{q} + \mathbf{s}(\mathbf{q}, t), \quad (\text{B7})$$

where  $\mathbf{s}(\mathbf{q}, t)$  is the displacement field which verifies

$$\frac{\partial^2 \mathbf{s}}{\partial t^2} + 2H \frac{\partial \mathbf{s}}{\partial t} = -\nabla \phi, \quad (\text{B8})$$

and  $\phi$  is the gravitational potential that satisfies  $\Delta \phi = 4\pi G \delta(r)$ . The ZA approximates the displacement field by its initial value  $\mathbf{s}(\chi_i, t) = \mathbf{s}_0(\mathbf{q})D(t)$  where  $D(t)$  is the linear growth factor which verifies equation (B4) and  $\mathbf{s}_0 = -(2\nabla \phi_0)/(3H_i^2 \Omega_{m,i})$ .

If we define  $\chi_i$  such as  $\chi(\mathbf{q}, t_i) = \chi_i$ , then  $\chi(\chi_i, t) = \chi_i + \mathbf{s}(\mathbf{q}, t) - \mathbf{s}_0(\mathbf{q})$ . Using equation (71), we can write explicitly  $\mathbf{s}_0(\mathbf{q})$  in the spherical approximation. It then follows that

$$\chi = \chi_i \left( 1 - \frac{\Delta_i}{3} \left[ \frac{D(t)}{D(t_i)} - 1 \right] \right), \quad (\text{B9})$$

which is exactly the solution obtained in equation (B6). This is not surprising since the ZA is by construction the first-order Lagrangian perturbation theory, we re-find it here in spherical geometry.

This paper has been typeset from a  $\text{\TeX/L\AA\TeX}$  file prepared by the author.